Recent Advances in Stratification and Film Formation of Latex Films; Attenuated Total Reflection and Step-Scan Photoacoustic FTIR Spectroscopic Studies

BOR-J. NIU, MAREK W. URBAN

Department of Polymers and Coatings, North Dakota State University, Fargo, North Dakota

Received 2 September 1997; accepted 3 December 1997

ABSTRACT: Surfactant–latex molecular level interactions as well as transient effects during latex film formation play an important role in latex technology. This review article focuses on the siloxane effects on anionic sodium dioctylsulfosuccinate (SDOSS) surfactant exudation during latex coalescence and quantitative analysis of SDOSS distribution at the both film–air (F–A) and film–substrate (F–S) interfaces. Attenuated total reflection (ATR) Fourier transform infrared (FTIR) spectroscopy was utilized for characterization of the interactions between SDOSS and styrene–butyl acrylate latex copolymers. In addition, studies of SDOSS stratification along with depth-profiling analysis during latex film formation utilizing step-scan photoacoustic (S^2-PAS) FTIR spectroscopy illustrate that SDOSS content is enriched at the F–A interface and decreases as the penetration depth increases across the latex film thickness. © 1998 John Wiley & Sons, Inc. J Appl Polym Sci 70: 1321–1348, 1998

Key words: latex coalescence; stratification; ATR and photoacoustic FTIR; surface depth profiling

LATEX COALESCENCE AND FILM FORMATION

Typical synthetic latex polymers consist of polymeric spheres, colloidally suspended in water,[1] with a milky, opaque appearance. Film formation from a polymer latex is a complexed, multistage phenomenon. Upon coalescence, some latexes can form transparent, tough, and continuous films, while others can be friable, opaque, and discontinuous. Regardless of the factors affecting the final film properties, to obtain a continuous latex film, the latex particles should diffuse into each other. Although this simplistic view is far more complex, and several attempts were made to understand a mechanism of the latex film formation in the past few decades, no conclusive results were obtained.

Dillon et al.[2] postulated that main contributions toward particle coalescence are provided by the polymer surface tension forces exerted, as the total surface area of the latex polymer decreases very greatly. This is schematically illustrated in Figure 1(A). To describe the coalescence of the latex polymer by viscous flow, the Frenkel equation,[1] $\theta^2 = (3\gamma t)/(2\pi r\eta)$ was applied, where θ is the degree of coalescence; γ, the surface tension (dyne/cm); t, the time (s); r, the particle radius (cm); and η, the particle viscosity (dyne-s/cm^2). Since for a given latex, γ, t, and η are constant and do not vary from particle to particle, the θ^2 term is proportional to $(1/r)$. Because it is difficult

Correspondence to: M. W. Urban.

This paper was presented at the National American Chemical Society Meeting in San Francisco, CA, in honor of Prof. Jack L. Koenig, the 1997 recipient of the Philips Award in Polymer Science.

Contract grant sponsor: National Science Foundation Coating Center.

Journal of Applied Polymer Science, Vol. 70, 1321–1348 (1998)
 CCC 0021-8995/98/071321-28

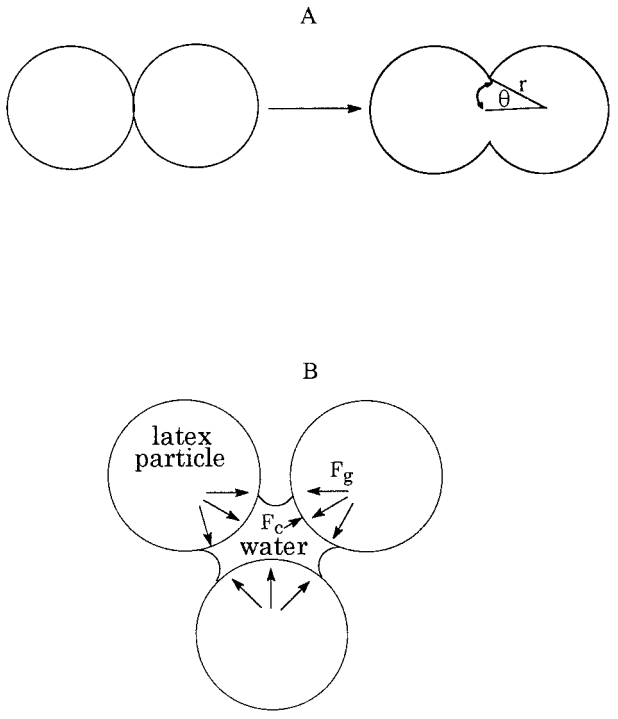

Figure 1 Driving forces for latex particles to coalesce: (A) Coalescence of latex particles by viscous flow; (B) contracting forces resulting from capillary water in particle interstices.

to measure γ accurately, these studies assumed that during drying each particle coalesced with the substrate to the same extent, as with another particle. Therefore, it was concluded that coalescence occurs by a viscous flow, with the polymer surface tension's being the driving force.

Brown[3] also postulated that these forces which arise from the polymer–water interfacial tension, while certainly operative, do not furnish the principal contribution of energy for the film-formation process. According to this approach, a capillary force, F_c, results from the surface tension of water, and evaporation causes the formation of very small radii of curvature among the particles. According to this hypothesis, coalescence occurs when F_c exceeds the force resisting deformation, F_g. This is schematically illustrated in Figure 1(B). Protzman and Brown also introduced the concept of the maximum modulus for the film formation, and the rate of water removal may determine the coalescence of borderline film formers; porous, incompletely coalesced films are formed by maintaining temperature below a minimum temperature required for the film formation.[4]

Although one could argue about the exact description of the coalescence mechanisms, most agree that the film-formation process can be divided into several distinct stages separated by distinct transitions.[5–8] They are schematically illustrated in Figure 2. Stage I is a wet stage shortly after latex deposition. Evaporation of water leads to Stage II, in which the particles first come into contact with each other, forming a close-packed array with water-filled interstices. During the transition to the next stage, loss of the interstitial water coincides with the particle deformation and compaction. Stage III can be envisioned as a dense array of individual particles which retain their identity. Finally, diffusion

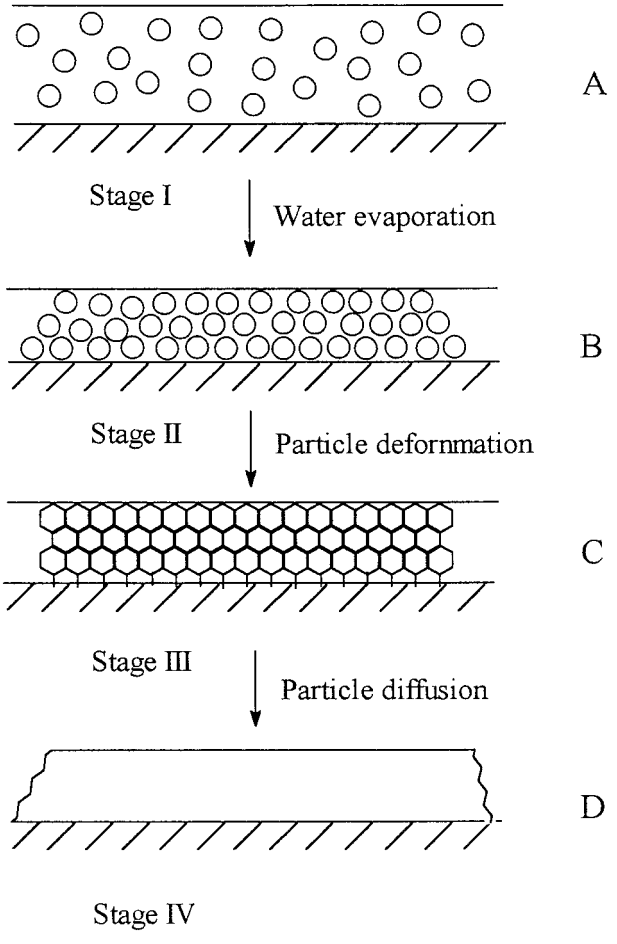

Figure 2 Schematic diagram of latex film formation: (A) Stage I, latex particles dispersed in H_2O; (B) stage II, latex particles contact each other; (C) stage III, latex particles deformation; (D) stage IV, coalesced latex film (continuous phase).

across the particle–particle boundaries leads to a homogeneous, continuous film, which defines Stage IV.

Utilizing a variety of different techniques, numerous studies have been conducted on individual stages. For example, Haas-Bar Ilan et al.[9] used vitreous preparation transition electron microscopy (TEM) to investigate concentrated aqueous dispersions of polystyrene latex at the early stages of coalescence. Recently, atomic force microscopy[10,11] (AFM) was utilized to observe surface topography and packing of the poly(butyl methacrylate) system during stage III. Small-angle neutron scattering (SANS),[12–17] nonraditative energy transfer (NET),[18–21] and scanning electron microscopy (SEM)[1,22,23] techniques were also utilized to study the molecular interdiffusion phenomena and microstructures in stages III and IV, respectively. If the temperature exceeds the minimum film-formation temperature of the system, clear, transparent, and void-free films will be formed. Most recent studies have shown that the mechanism of film formation depends upon the structure of the latex particles and the makeup of the dispersion.[23,24] In the past, a major emphasis was given to such factors[1] affecting film formation as polymer surface tension,[2] particle size and capillary forces between particles,[3] as well as diffusion.[2,25] However, the role of low molecular weight surfactants and other emulsifiers during and after the latex film formation and their behavior was investigated[26–37] only recently.

Although monodispersity and the particle-size diameter are essential factors determining film properties, it is also important to establish interactions between individual latex components. In this case, spectroscopic techniques are usually employed since information on the molecular level is sought. Among spectroscopic techniques, Fourier transform infrared (FTIR) spectroscopy had found only limited application to latex systems in the past, mainly because of the strong absorbance of water in the infrared region. Recently, Evanson and Urban[26–28] demonstrated the surfactant migration in latex films by attenuated total reflection (ATR) FTIR. Surfactant enrichment at both the film–air (F–A) and film–substrate (F–S) interfaces was observed. Furthermore, analysis of surfactant exudation in the early stage of coalescence as well as interactions between polymers and other components of the latex system was achieved.

Since properties of latex films may be influenced by the surface activity of surfactants, determination of the surface activity of surfactant throughout the latex film is essential and plays a significant role in the film properties, such as adhesion, durability, and other physical properties. Especially, the latex composition at the F–A and F–S interfaces is of particular interest. These reasons motivated further investigation into the distribution of surfactants throughout latex films during film formation. Urban and Evanson[26] demonstrated that the sodium dioctylsulfosuccinate (SDOSS) anionic surfactant can interact with latex polymers. To understand the origin of the surface surfactant–copolymer interactions, analysis of two bands at 1056 and 1046 cm^{-1} was important since they appear to be sensitive to the SO_3^- Na^+ environments. Both bands originate from the symmetric S—O stretching vibration of the SO_3^- groups, and because the copolymer contained carboxylic acid groups, hydrogen bonding between the carboxylic acid and the sulfonate groups or ionic interactions are most likely responsible for the occurrence of the two infrared bands in this region, resulting in that the band at 1056 cm^{-1} is attributed to the hydrogen-bonding interactions between sulfonate groups and copolymer, SO_3^- $Na^+\cdots$HOOC, and the band at 1046 cm^{-1} is due to the hydrogen-bonding interactions between sulfonate groups and H_2O, SO_3^- $Na^+\cdots H_2O$. Evanson and Urban[27] also demonstrated that the surfactant exudation was influenced by the surface tension of substrate. Figure 3 depicts the anionic surfactant behavior on the three substrates. Latex films prepared on polytetrafloroethylene (PTFE) exhibit moderate exudation of SDOSS to the F–S interface in order to lower the interfacial surface tension between the copolymer and the PTFE; however, the films prepared on glass (KRS-5) exhibit minimal or no exudation to the F–S interface. This is because copolymer is able to wet the substrate, thus lowering the driving force for SDOSS exudation to this interface. In the case of the latex films prepared on mercury, the enhancement of surfactant exudation to the F–S interface is attributed to the fact that a liquid will only wet a surface of higher surface energy. Therefore, if the latex is deposited on a liquid Hg substrate, there are two liquids in contact with each other. Initial surfactant enrichment may occur to lower the surface tension at the liquid–liquid interface. As the coalescence progresses, water evaporates, leaving the copolymer film in contact with the mercury and forming a solid (latex film)–liquid (Hg) interface. Because mercury has a high surface energy, a high inter-

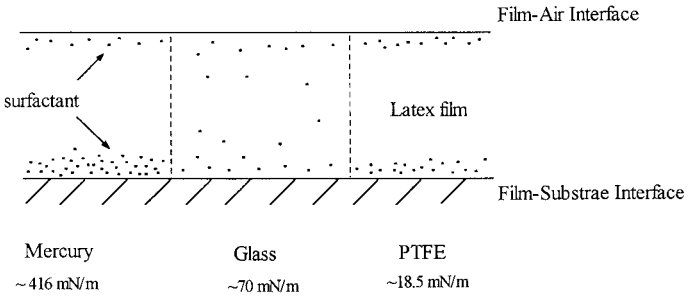

Figure 3 Schematic diagram of the surface tension effect on the surfactant exudation across the latex film prepared from mercury, glass, and PTFE substrates.

facial surface tension exists at this interface, providing a sufficient driving force for the surfactant to exudate to this interface. In an effort to establish how the interfacial surface tension may affect surfactant mobility, the interfacial surface tension values are listed in Table I.[29] Based on the values on Table I, it is apparent that the surfactant exudation is driven by an initial high interfacial (water–substrate) surface tension difference.

Studies on the role of low molecular weight surfactants during the latex film formation is particularly important since polymeric systems often contain low molecular weight components that are purposely added either to facilitate polymer synthesis, for stabilization purposes, or to improve the film formation. In the case of latexes, it is a surfactant molecule, that upon addition to a reaction mixture, facilitates the environment conducive to the polymerization of high molecular weight polymer particles, as well as their stabilization in an aqueous medium. Due to the fact that surfactant molecules remain in the latex suspension prior to coalescence, their presence modifies the latex film chemical properties and its physical integrity. Thus, such film properties as adhesion, environmental stability, or optical properties can be influenced by surfactant distribution throughout the film. Therefore, it is important to understand those factors that govern surfactant distribution and structural characteristic features near surfaces and interfaces of latex films.

Table I Estimated Interfacial Surface Tensions

	Interfacial Surface Tension (mN/m)	
	γ_{int} (water)	γ_{int} (film)
Substrate		
Mercury	416	351
Glass	60	0.5
PTFE	50	1.25

SURFACTANT BEHAVIOR IN LATEX FILMS

Although several attempts to explain the role and behavior of surfactants in latex films have been made, none of them provided satisfactory understanding of the surfactant behavior.[38–44] Okubo et al.[45] also showed that ethyl acrylate/methyl methacrylate copolymer latex films decreased in permeability as the sodium dodecyl benzene sulfonate (SDBS) concentration was increased. The reduction of permeability of latex films may be a result of morphological changes in the film because the addition of a hydrophilic surfactant is expected to increase permeability. The added surfactant could play two roles during the film formation: First, it would give the particle greater stability, and, hence, the particles would be in a more ordered state, preventing coagulation, and, second, the surfactant could plasticize the particle surface, resulting in a greater degree of coalescence during the film formation. Isaacs[46] also demonstrated that more ordered films were found when the latex stability was improved by surfactant addition.

Evanson and Urban,[26,27,29] Evanson et al.,[28] and Thorstenson and Urban[30] showed that the exudation of surfactants is also influenced by other factors. For example, in ethyl acrylate/methacrylic (EA/MAA) acid latex, surfactant molecules tend to exude toward the F–S interface when coalescence was conducted on a high surface tension substrate. This behavior was attributed to the surface tension difference between the substrate and the latex. Thorstenson et al.,[31–33]

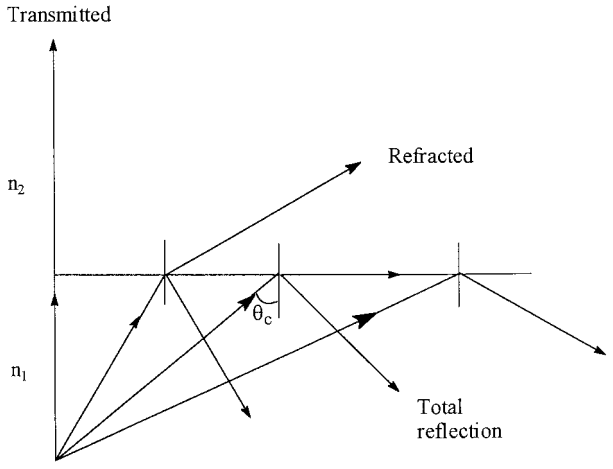

Figure 4 Schematic diagram of the effect of refractive index changes on the light path as a function of incidence angle. (From Urban, M. W., *Vib. Spect. Mol. & Macromol. on Surf.,* pp. 00–00, © 1994 John Wiley & Sons, Inc., reproduced with permission.)

Kunkel and Urban,[34] Niu and Urban,[35,36] and Tebelius and Urban[37] also demonstrated that the polar sulfonate groups of the SDOSS surfactant can interact with the carboxylic acid functionality of the copolymer and these interactions are affected by the residual water present in the film after coalescence.

Orientation and spatial distribution of acid functionalities were examined,[33] showing that dimeric carboxylic acid species can assemble at the interface between latex films and a substrate. Dimeric acid entities were found to be preferentially parallel to the interface, and "aging" of the latex aqueous suspension causes excessive exudation of surfactant molecules to the F–A interface.[34] Upon exudation to the surface, the hydrophilic SO_3^- Na^+ groups assemble in preferentially normal-to-the-surface direction, whereas hydrophobic tails are randomly buried in the latex film. In the mixture of polystyrene and poly(*n*-butyl acrylate) latexes, more surfactant molecules exude to the F–A interface and less to the F–S interface.

In an effort to establish to what extent transient effects prior to coalescence may influence mobility, distribution, and orientation of surfactant molecules after coalescence, polystyrene (Sty) and poly(*n*-butyl acrylate) (*n*-BA) were mixed independently in a 1 : 5 ratio, and the mixture was allowed to stabilize prior to coalescence.[35] It appears that the latex stabilization may have a significant effect on the distribution of surfactant molecules across the coalesced latex and that their orientation changes depend upon the stage of coalescence and the water front's moving toward the surface. In these studies, it also became apparent that vibrational spectroscopy, in particular, ATR and step-scan photoacoustic (S^2-PAS) FTIR spectroscopy, is a powerful tool in determining molecular level features occurring near interfacial regions in latex films.

ATR FTIR SPECTROSCOPY

To obtain molecular-level information from surfaces of polymeric films, internal reflection spectroscopy (IRS) was introduced.[47,48] When light passes through two media having different refractive indices and the media are in contact with each other, the path of the light is distorted. This is schematically illustrated in Figure 4. The majority of light is transmitted at a 90° angle of incidence (θ), and the light is partially reflected at $\theta < \theta_c$. A total reflection will occur at $\theta > \theta_c$. When the angle of incidence θ is greater than θ_c, the light is totally reflected.[48,49] The critical angle is defined by $\theta_c = \sin^{-1} n_2/n_1$, and n_1 and n_2 are the refractive indices of a crystal and a sample, respectively. This is the basis for IRS.[50,51]

IRS can be used to measure the optical spectrum of sample that is in contact with an optically denser and transparent medium. The original single-reflection method was developed by Fahrenfort.[52,53] Since there is only one reflection during the measurement, sensitivity is limited. Therefore, this technique was modified by increasing the number of reflections, giving rise to ATR spectroscopy.[54–58] Experimental setups of the internal reflection technique for single-reflection and multireflection methods is shown in Figure 5. One of the advantages of IRS is that it is

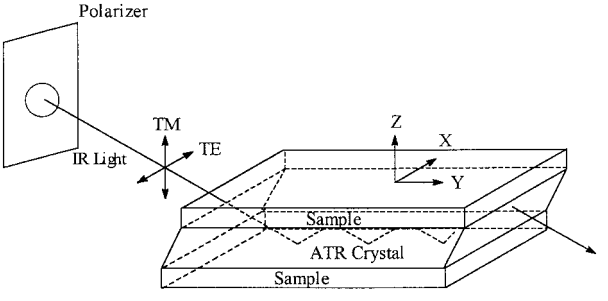

Figure 5 Schematic diagram of the polarized ATR FTIR elements.

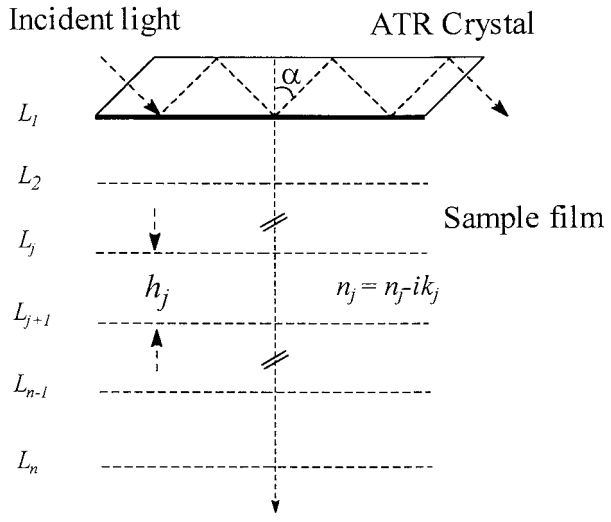

Figure 6 Schematic diagram of *numerically* slicing a nonhomogeneous surface to form a stack of parallel thin homogeneous layers. (Reproduced with permission from ref. 60. Copyright 1993 Society for Applied Spectroscopy.)

possible to conduct depth-penetration experiments. The penetration depth, d_p, is expressed by the following equation[47,48]:

$$d_p = \frac{\lambda}{2\pi(n_0^2 \sin^2 \theta - n^2)^{1/2}} \quad (1)$$

where d_p (cm) is the depth penetration into the surface; n_0 and n, the refractive index values of an ATR crystal and a sample, respectively; θ (degree), the angle of incidence; and λ (cm^{-1}), the wavelength of electromagnetic radiation.

As shown by eq. (1), one disadvantage for ATR FTIR spectroscopy is that the depth of penetration depends upon the wavenumber. To eliminate this effect, Huang and Urban[59,60] developed an algorithm to obtain the same levels of the depth penetrations across the spectrum. Because eq. (1) was derived with an assumption that the specimens examined are homogeneous, any composition/concentration variations preclude the use of this useful relationship for quantitative purposes, especially if one is interested in the depth-profiling experiments. For that reason, Huang and Urban[60] developed an algorithm capable of analyzing nonhomogeneous surfaces, which is schematically illustrated in Figure 6. The surface is divided into n layers with each layer thickness, h_j. At the each boundary layer, L_j, the response of the sample to local evanescent waves is characterized by a complex refractive index defined by $\hat{n}_j = n_j - ik_j$, and n_j is the refractive index, where k_j is referred to as the absorption index.[59] to each layer, which is assumed to be homogeneous, eq. (1) can be utilized. However, the layers among themselves are not homogeneous, and by stacking all layers together, the surface is reconstructed by a stepwise treatment of volumes occupied by each layer.

This approach allows quite accurate quantitative analysis of surfaces, and its precision is determined by the number of spectra collected at various depths. Based on this principle, quantitative analysis of the surfactant concentration near the F–A and F–S interfaces can be examined in coalesced latex films. Furthermore, by incorporating polarized IR light in an ATR experiment, it is possible to determine orientation of the surface species. The diagram of polarized ATR FTIR experimental setup is schematically illustrated in Figure 5.

PHOTOACOUSTIC (PA) AND PHOTOACOUSTICS STEP-SCAN FOURIER TRANSFORM SPECTROSCOPY

Photoacoustic spectroscopy is based on the detection of an acoustic signal emitted from a specimen due to absorption of modulated radiation. This is schematically illustrated in Figure 7(A). The sample is placed in an acoustically isolated chamber to which a sensitive microphone is attached. Upon absorption of modulated light, heat is generated within the sample. Its release leads to temperature fluctuations at the sample surface, which subsequently causes pressure changes in a surrounding gas, thus generating acoustic waves in the sample chamber at the frequency of the modulated light. The pressure changes of the gas are detected by a sensitive microphone, and the obtained electrical signal is Fourier-transformed.

In the PAS experiment, the absorbed energy is released in a form of heat that is transferred to the sample surface, and the efficiency of the heat transfer is determined by the thermal diffusion coefficient of the sample, a_s(cm), and the modulation frequency of the incident radiation, ω[61,62]:

$$a_s = \left(\frac{\omega}{2\alpha}\right)^{1/2} \quad (2)$$

where α (cm^2/s) is the thermal diffusivity and ω (s^{-1}) is the angular modulation frequency and

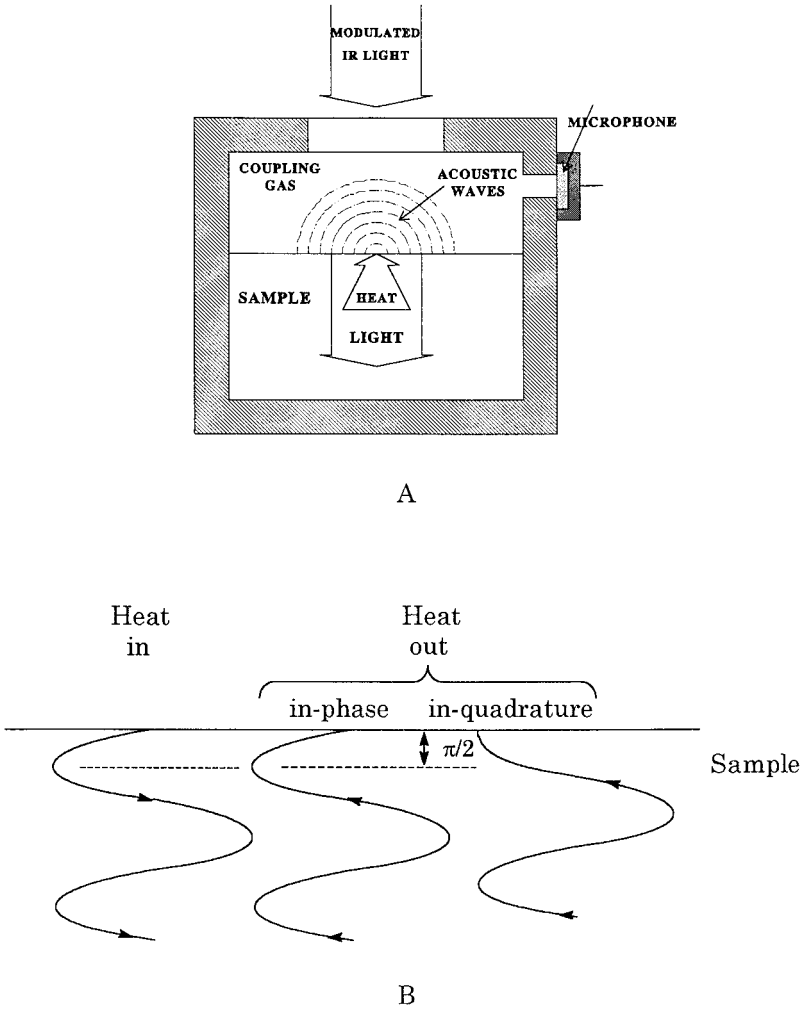

Figure 7 (A) Schematic diagram of step-scan photoacoustic cell; (B) schematic diagram of two components of in-phase and in-quadrature in step-scan phase analysis.

equal to $2\pi v\nu$ [v, (cm/s) and ν (cm^{-1}) are velocity of mirror and wavenumbers, respectively). The thermal diffusion length μ_{th} (cm) is related to the thermal diffusion coefficient a_s through

$$\mu_{th} = \frac{1}{a_s} = \left(\frac{2\alpha}{\omega}\right)^{1/2} \tag{3}$$

Based on this relationship, the thermal diffusion length is inversely proportional to the modulation frequency. Therefore, by changing ω, one changes μ_{th}, which, in effect, changes the depth from which the acoustic signal is generated to the surface. Thus, the capability of surface depth profiling is one of the most appealing features of PA FTIR. Urban[63] and Urban and Koenig[64] demonstrated the several applications of PAS in surface depth-profiling studies and the orientation of the surface species. However, the major drawback of this setup is that the thermal diffusion length also depends on the wavenumber. As a result, the low wavenumber region provides deeper penetration depths, and for the high wavenumbers, the spectral information comes from shallower depths. To eliminate this wavenumber dependence and obtain a penetration depth wavenumber-independent spectra, step-scan photoacoustic FTIR spectroscopy can be employed.

In a step-scan interferometry, a mirror of an interferometer is moved incrementally, and the data are acquired while the retardation is constant. The result is that the Fourier frequency dependence is eliminated. A single frequency of modulation can be imposed on the IR beam, which

applies to all wavenumbers in the spectra. As a result, the photoacoustic sampling depth is constant across the spectrum. Furthermore, using a digital signal processor (DSP) to precisely control the mirror position, in-phase and in-quadrature components of the signal can be simultaneously acquired and used to obtain the signal phase.

In a step-scan PA FTIR spectrometer, the modulation can be introduced with amplitude (AM) and phase (PM) modulations. Amplitude modulation is introduced by a chopper to generate the PA signal.[65,66] The disadvantage for amplitude modulation is that it produces a signal containing a large dc component. In the phase modulation, the retardation is varied by dithering the mirror at a fixed frequency. There are two major advantages of the phase modulation over amplitude modulation in the step-scan PAS FT-IR spectroscopy: First, the use of PM rather than AM for a signal generation increases the step-scan signal-to-noise ratio (SNR) twofold. Second, the amplitude of PM can be used to select the wavelength region most efficiently modulated. Thus, the step-scan mode, particularly in conjunction with PM, provides a constant frequency modulation for all wavelengths.

Because of the discrete modulation frequency, PA signal phase information is easily obtained by recording two orthogonal components of the signal, in-phase and in-quadrature, with a digital signal processor. Bertrand[67] demonstrated the application of step-scan phase analysis to thermally thin, weakly absorbing surface layers and compared it to a thermally thick, weakly absorbing substrate. In this case, the two spectra were separated by a 45° phase difference. In considering the use of PA phase data for the depth-profiling experiments, it is important to know that the concept of the thermal diffusion depth is applicable to homogeneous materials.

For nonhomogeneous polymers, the PA probe depth and phase characteristics may differ from the conventional mode. On the other hand, the 45° phase difference may not hold, and the range of signal phase from 0° to 90° can be observed.[68] In general, bands recorded in the step-scan photoacoustic mode from deeper layers will show a longer phase lag than will those from shallow layers. The use of phase analysis along with variation of the modulation frequency increases the power of the depth-profiling studies, particularly if several discrete modulation frequencies can be applied simultaneously.[69]

Using phase analysis, two different phases, due to the differences in penetration lag, can be detected, and the in-phase and in-quadrature spectra can be collected. Schematic diagrams of the step-scan PAS cell and the in-phase and in-quadrature phase are illustrated in Figure 7(A,B). Palmer and Dittmar[70] and Gregoriou et al.[71] indicated that the depth information of two thin films, cobalt tetraphenylporphrin and hexamethyldisilazane, deposited on the polypropylene can be obtained by changing the modulation frequency. Furthermore, the combination of modulation-frequency variation and phase analysis are also utilized to distinguish multiple layers. Bertrand[67] also demonstrated that the absorption coefficient, β, of polymeric materials can be measured from the phase analysis. Since $\beta\mu$ is obtained from the following equation:

$$\beta_\mu = \frac{P_{\mathrm{Qu}} - P_{\mathrm{Ph}}}{P_{\mathrm{Ph}}} \tag{4}$$

where β (cm^{-1}) is the absorption coefficient; μ (cm), the thermal diffusion length; and P_{Qu} (photoacoustic signal, V) and P_{Ph} (photoacoustic signal, V), the in-quadrature and the in-phase, respectively, components of the PAS signal. Since the μ is constant in step-scan PAS FTIR, the β can be obtained from the product of $\beta\mu$. With this background in mind, we will discuss several studies utilizing ATR and step-scan PAS FTIR spectroscopy that allowed us determination of structure–property relationships at the F–A and F–S interfaces, in particular, with the current developments in 2-D spectroscopy.[72,73]

SILOXANE EFFECTS ON SDOSS SURFACTANT MIGRATION

Silicone-containing latexes are known for their outstanding thermal and photolytic stabilities. In general, their heat and weather resistance are closely related to the amount of a silicone content in a given polymer network.[74] Furthermore, when silanes are added to a coating formulation, they are known to improve numerous properties. For that reason, silanes in their hydrolyzed form added to latex suspensions may result in a coalesced polymer network with significantly altered properties. If one believes that interpenetrating networks (IPN) exist, the IPN term would be used to describe such polymers, in which silane sub-

networks are interpenetrated by entanglements of high molecular weight copolymers.[75] However, when such silanes are added to an aqueous suspension, reactions of these species in the latex aqueous suspensions usually involves hydrolysis of siloxane groups, leading to the silanol formation, followed by silanol condensation, which may occur on surfaces of latex particles. Finally, if the surface reactions are favorable, a crosslinked polymer network is formed after coalescence.[76] Figure 8 illustrates schematically how silanes may become incorporated into a latex network.

Niu and Urban[35] demonstrated that there is a significant influence of interfaces on mobility of small molecules in latex films. As a result, various properties, including adhesion, durability, and thermal resistance, may be affected. Since the presence of silanes may inherently alter already attractive properties of latexes, this issue stimulated us to expand the scope of our research program and examine the behavior of SDOSS in Sty/*n*-BA latexes containing silanes such as trimethoxysilyl propyl methacrylate with a formula of $H_2CCCH_3COOCH_2CH_2CH_2Si(OCH_3)_3$ (MSMA).

Figure 9 illustrates a series of ATR FTIR spectra recorded from the F–S interfaces of the latex films composed of 100% poly(*n*-BA) and 50%/50% Sty/*n*-BA. This choice of composition was dictated by the compatibility differences between Sty and *n*-BA components with respect to SDOSS and the glass transition temperatures of latex polymers. Traces A and C of Figure 9 illustrate the spectra of 100% *n*-BA without (trace A) and with MSMA (trace C). It is apparent that the bands at 1326, 1298, and 1202 cm^{-1} are detected when the latex contains MSMA. These bands are attributed to the in-plane $H_2C{=}C$ deformation (1326 and 1298 cm^{-1}) and $Si{-}CH_2$ symmetric stretching (1202 cm^{-1}) modes of MSMA. When the latex glass transition temperature is increased by changing its composition to 50%/50% Sty/*n*-BA, the bands due to MSMA become more pronounced, indicating that a higher content of MSMA is detected near the F–S interface. This is demonstrated by the presence of significantly stronger MSMA bands at 1326, 1298, and 1202 cm^{-1} (trace D, Fig. 9). Figure 10 shows ATR FTIR spectra of the same specimens, but in the S—O stretching region. As we recall, our previous studies[26–35] indicated two bands at 1046 and 1056 cm^{-1}, which are attributed to the S—O bands resulting from H-bonding associations of the S—O bonds with H_2O molecules and COOH groups on latex surface, respectively. A comparison of traces A and C of Figure 10 indicates that, when MSMA is added to 100% *n*-BA latex formulation, the 1056 and 1046 cm^{-1} bands are not detected. The band at 1056 cm^{-1} is not detected at all, regardless of the presence of MSMA.

Since 1046 cm^{-1} band results from the SO_3^- Na^+ and H_2O interactions, the presence of MSMA causes the displacement of SDOSS molecules from the F–S interface. To identify the origin of this phenomenon, let us realize that the presence of the 1056 cm^{-1} band was found to be a function of two factors: a particle size and a latex particle composition.[35] As we recall our previous studies[35] conducted on 50%/50% Sty/*n*-BA latexes with the particle sizes of 100 and 50 nm, the 1056 cm^{-1} was detected only for latexes with 100-nm particles. In this study, we also used a 50-nm particle latex, and the 1056 cm^{-1} was also not detected.

To understand how a particle size would alter SO_3^- Na^+ ···HOOC interactions, let us realize that a larger latex particle size is accomplished by slower stirring of the reaction mixture during latex polymerization. Under such circumstances, the reactivity ratio of the starting monomers will have a major influence on a latex particle composition. As we already established in our previous studies and discussed in the context of the reactivity ratios for Sty and *n*-BA published in the literature,[34] the reactivity ratios of styrene and *n*-BA favor homopolymerization of styrene. As a result, preferential formation of a polystyrene core and poly(*n*-BA) shell is anticipated. If this is the case, there is a sufficient amount of COOH groups available for interactions with hydrophilic ends of SDOSS, and the 1056-cm^{-1} band is detected.

A smaller particle size can be achieved by a vigorous stirring of polymerizing suspension, which subsequently will diminish the influence of reactivity ratios during latex polymerization, thus enhancing the probability of random copolymerization. Therefore, using the same composition of the starting materials, smaller particles with more uniform distribution of Sty/*n*-BA within each particle will be produced. Hence, a fewer COOH species will be available for H bonding with SO_3^- Na^+ hydrophilic SDOSS ends.

To further justify that the particle size may affect the presence of acid groups near the surface, a mixture of 50%/50% w/w of poly(Sty) and poly(*n*-BA) homopolymerized latexes in separate batches was allowed to coalesce. In this case, the band at 1056 cm^{-1} is present (Fig. 11, trace A). In contrast, the ATR spectrum of pure SDOSS shows

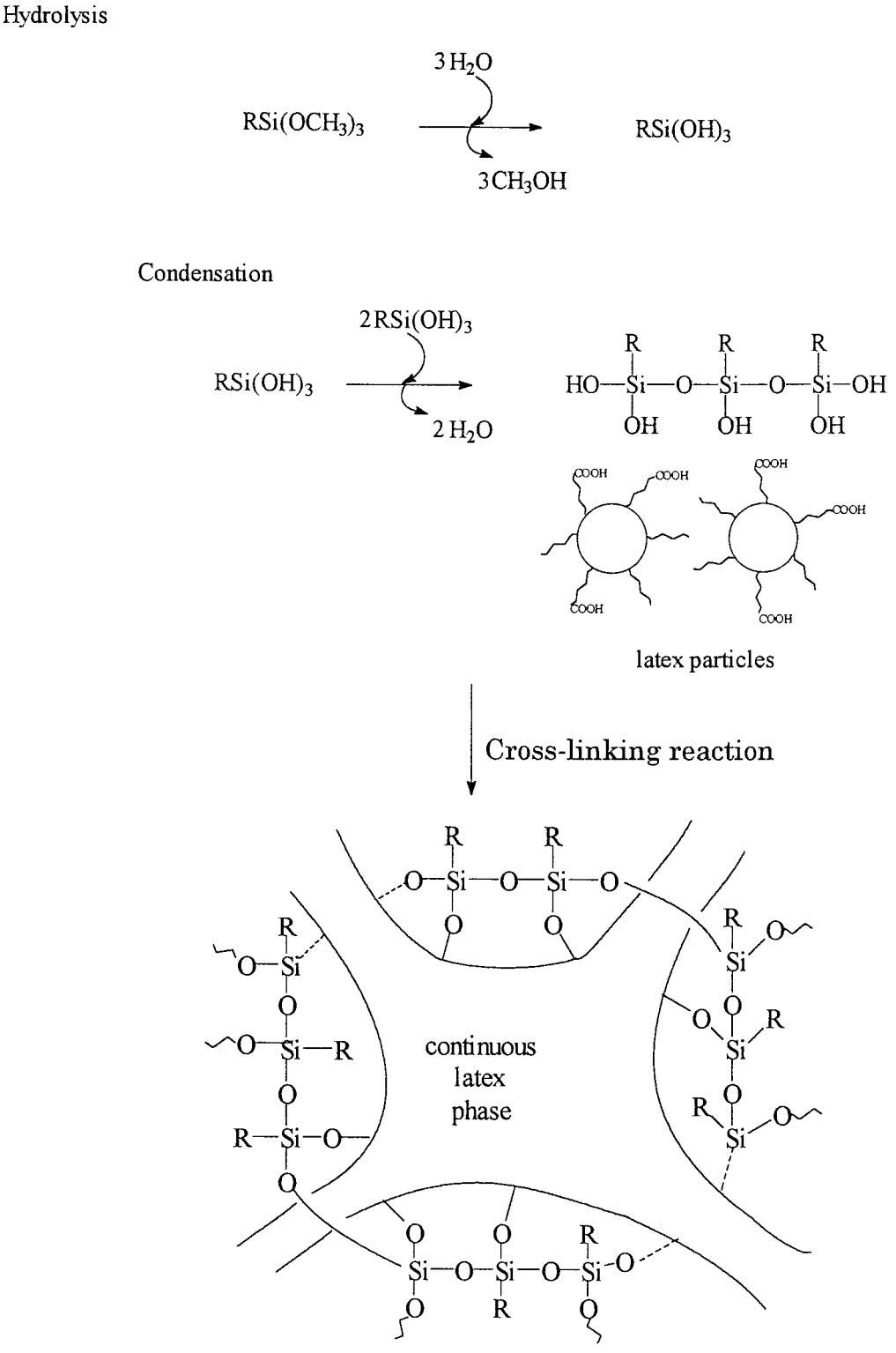

Figure 8 Schematic diagram of reaction mechanism for silicone modifiers during latex coalescence. (From Witucki, G. L., *J. Coat. Tech.*, **65,** 57, © 1996 John Wiley & Sons, Inc., reproduced with permission.)

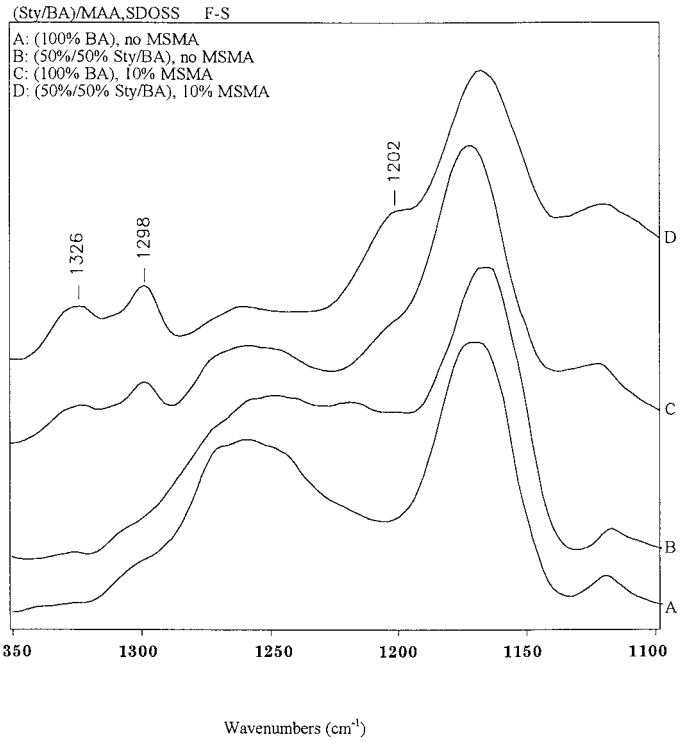

Figure 9 ATR FTIR spectra of various Sty/*n*-BA latex copolymers with and without MSMA in S—O asymmetric stretching vibrational modes at F–S interface: (A) 100% *n*-BA without MSMA; (B) 50/50% Sty/*n*-BA without MSMA; (C) 100% *n*-BA with MSMA; (D) 50/50% Sty/*n*-BA with MSMA. (From Witucki, G. L., *J. Coat Tech.,* **65,** 57, © 1996 John Wiley & Sons, Inc., reproduced with permission.)

that only the 1050-cm^{-1} band is detected. This is shown in Figure 11, trace B. This observation indicates that, for the same particle-size homopolymers of polySty and poly(*n*-BA), either there are islands of poly(*n*-BA), which allow for the SO_3^- Na^+ and COOH groups to interact with each other, or there is an access of poly(*n*-BA) near the latex film surface, allowing for the same type of interactions. Based on these observations, for a large Sty/*n*-BA particle size, there is a higher *n*-BA content near the latex surface particle, whereas for a smaller particle size, more uniform distribution is anticipated. Figure 12 illustrates how the effect of particle size may influence the Sty/*n*-BA distribution after coalescence.

Having identified the effect of the particle size and the particle composition on SDOSS···HOOC interactions, let us go back to the issue of displacement of SDOSS molecules by MSMA from the interfaces. This phenomenon is particularly pronounced for the 50%/50% Sty/*n*-BA latex copolymer composition in Figure 9, trace D. To understand this behavior, it should be realized that the compatibility among latex components and free volume may play a significant role. For example, 50%/50% Sty/*n*-BA latex exhibits higher glass transition temperature; thus, it exhibits a lesser amount of the free volume at a given temperature. Therefore, the ability to diffuse due to the free-volume differences and compatibility among the components will play a significant role.

For example, poly(*n*-BA) is more compatible with MSMA than with 50%/50% Sty/*n*-BA. In view of these considerations and the fact that SDOSS is displaced from the F–S interface by MSMA molecules, which may form a network between the latex particles, fewer MSMA molecules are available for crosslinking during latex coalescence. As a result, less pronounced band intensities at 1326, 1298, and 1202 cm^{-1} are detected for 100% *n*-BA latex (trace C). However, their increase is detected for 50%/50% Sty/*n*-BA, which is illustrated in Figure 9, traces C and D, respectively, indicating that more MSMA molecules are grafted on the latex particles for a 50%/50% Sty/*n*-BA composition. Figure 13 shows a series of ATR FTIR spectra recorded from the F–A interface for 100% *n*-BA and 50%/50% Sty/*n*-BA la-

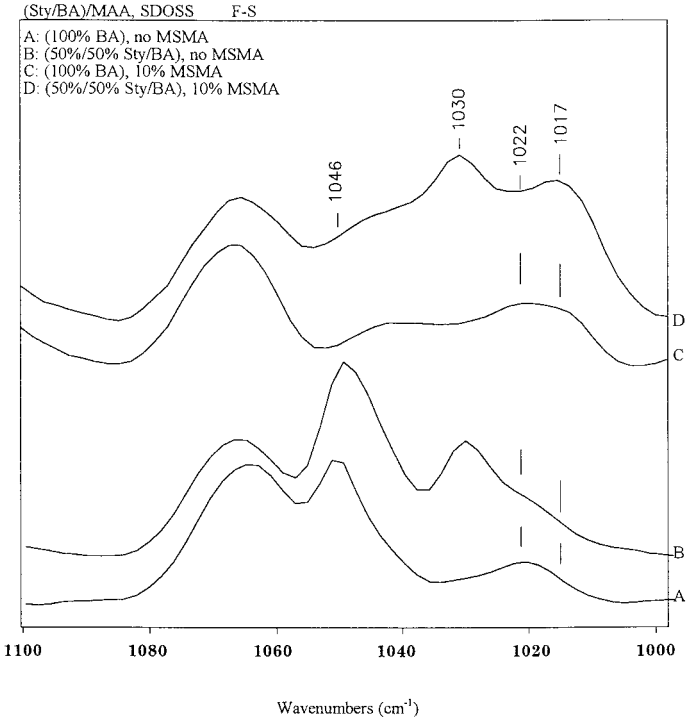

Figure 10 ATR FTIR spectra of various Sty/*n*-BA latex copolymers with and without MSMA in S—O symmetric stretching vibrational modes at F–S interface: (A) 100% *n*-BA without MSMA; (B) 50/50% Sty/*n*-BA without MSMA; (C) 100% *n*-BA with MSMA; (D) 50/50% Sty/*n*-BA with MSMA. (From Witucki, G. L., *J. Coat Tech.,* **65,** 57, © 1996 John Wiley & Sons, Inc., reproduced with permission.)

texes. In essence, these data resemble the data presented in Figure 9, and the only detectable difference is a marginally higher content of MSMA detected for a 50%/50% Sty/*n*-BA composition. However, as compared to the results for the same specimens at the F–S interface, the S—O stretching region of the F–A interface presented in Figure 14 shows a weaker S—O stretching band at 1046 cm^{-1} (traces B and D).

Furthermore, when MSMA is incorporated into the latex formulation, it appears that the 1017 cm^{-1} band increases. This is illustrated in traces C and D, Figure 14, and indicates that the Si—OCH_3 groups of MSMA hydrolyze and are able to become attached to the latex to form new Si—O—C linkages. This is demonstrated by the presence of the 1017-cm^{-1} band. As we recall the results presented in trace C of Figure 9, the band intensities at 1326, 1298, and 1202 cm^{-1} at the F–S interface are stronger than those at the F–A interface (Fig. 13, trace C). Although it is generally accepted that silanes tend to migrate to the F–S interface, which is illustrated in Figure 10(A), molecular level mechanisms responsible for MSMA diffusion are likely attributed to the formation of alkoxy silanes near the surface. After hydrolysis (Fig. 8), methoxy silanes are converted to hydroxyl groups, and during coalescence, the covalent bonds between hydroxyl groups on MSMA and latexes are formed near the F–S interface.

More SDOSS molecules are detected near the F–A interface in silicone-modified latex films. An opposite behavior was found for SDOSS exudation in the nonsilicone-modified latex films, and a higher content of SDOSS molecules was detected near the F–S interface. Let us return to the S—O and Si—O stretching regions recorded with TE polarization in Figure 15. Trace A shows that the 1046 and 1017 cm^{-1} bands, due to the S—O and Si—O stretching normal vibrations, respectively, are detectable with TE polarization. However, these bands are not detectable when the spectra are recorded with TM polarizations (Fig. 16, trace A). Because polarized ATR data allow us to establish orientation of the dipole moment changes with respect to a laboratory axes, the SO_3^- Na^+ hydrophilic end groups and Si—O groups in

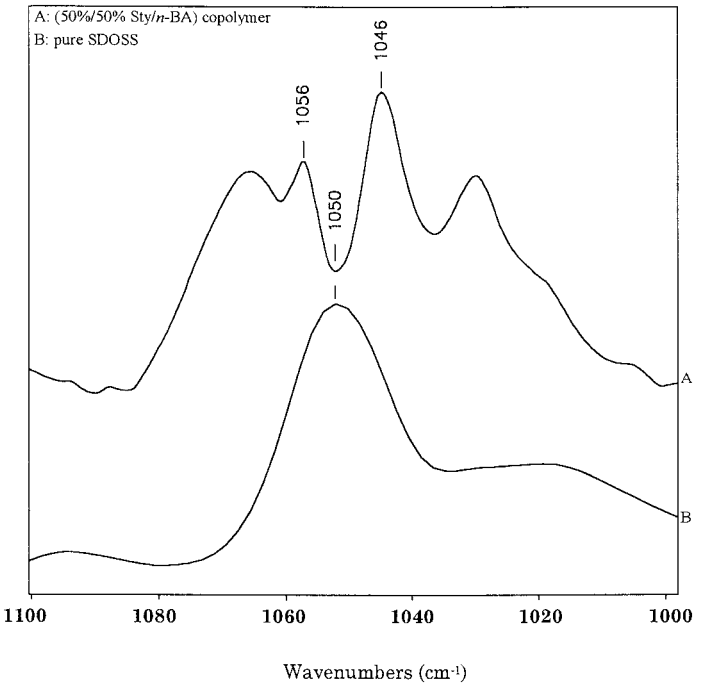

Figure 11 ATR FTIR spectra: (A) 50%/50% Sty/*n*-BA copolymer with a particle size at 100 nm; (B) pure SDOSS surfactant molecules. (From Witucki, G. L., *J. Coat Tech.,* **65,** 57, © 1996 John Wiley & Sons, Inc., reproduced with permission.)

MSMA are preferentially parallel to the film interfacial surface. The 1046-cm^{-1} band is enhanced in the TE polarization (Fig. 15) and this band is not detectable in the TM polarization (Fig. 16), indicating that the hydrophilic $SO_3^- Na^+$ ends are preferentially parallel to the F–S interface. Since the 1017-cm^{-1} band is only detected in the TE polarization (Fig. 15) and not detected with TM polarization (Fig. 16), MSMA molecules are preferentially parallel to the film surface. They are shown in Figure 17, marked as the F–S interface.

In conclusion, let us return to Figure 8 and realize that if the IPN is formed one would anticipate that there would be a uniform distribution of MSMA molecules across the film. However, the MSMA molecules are concentrated near the F–S interface, indicating that, if the IPN is formed, it would be highly localized. Therefore, these results show that there is a significant gradient of properties across the film thickness. As a matter of fact, these, as well as our previous[30–36,77] studies, indicated that the concept of IPN, or the phase separation within polymer networks forming polymeric films, is strongly affected by the film formation. There may be a significant difference in the network properties between the F–A and F–S interfaces.

QUANTITATIVE ANALYSIS OF SURFACTANT IN LATEXES

It appears that it is of primary interest to determine surfactant local concentration levels at the interfaces. However, the penetration depth is dependent upon the wavenumber, resulting in that the penetration depth is not constant in entire ATR spectrum. This disadvantage limits the application of ATR technique for quantitative analysis. To solve this problem, Huang and Urban[59,60] developed a Q-ATR algorithm with a double Kramers–Krong transform (KKT) to correct the optical constant, leading to that the quantitative analysis is more accurate and is able to be performed in the ATR technique. To quantify the concentration of SDOSS at the F–A and F–S interfaces, it is necessary to obtain extinction coefficients for the bands of interest, in our case the 1056- and 1046-cm^{-1} bands.[78] For that reason, the plots of the 1056- and 1046-cm^{-1} band intensities as a function of concentration of SDOSS were constructed and are shown in Figure 18(A,B). To minimize the optical effects from the Circle™ ATR spectra, all spectra were corrected using the Q-ATR algorithm,[59,60] subsequently allowing calculations of the extinction coefficients from the Beer–Lambert equation:

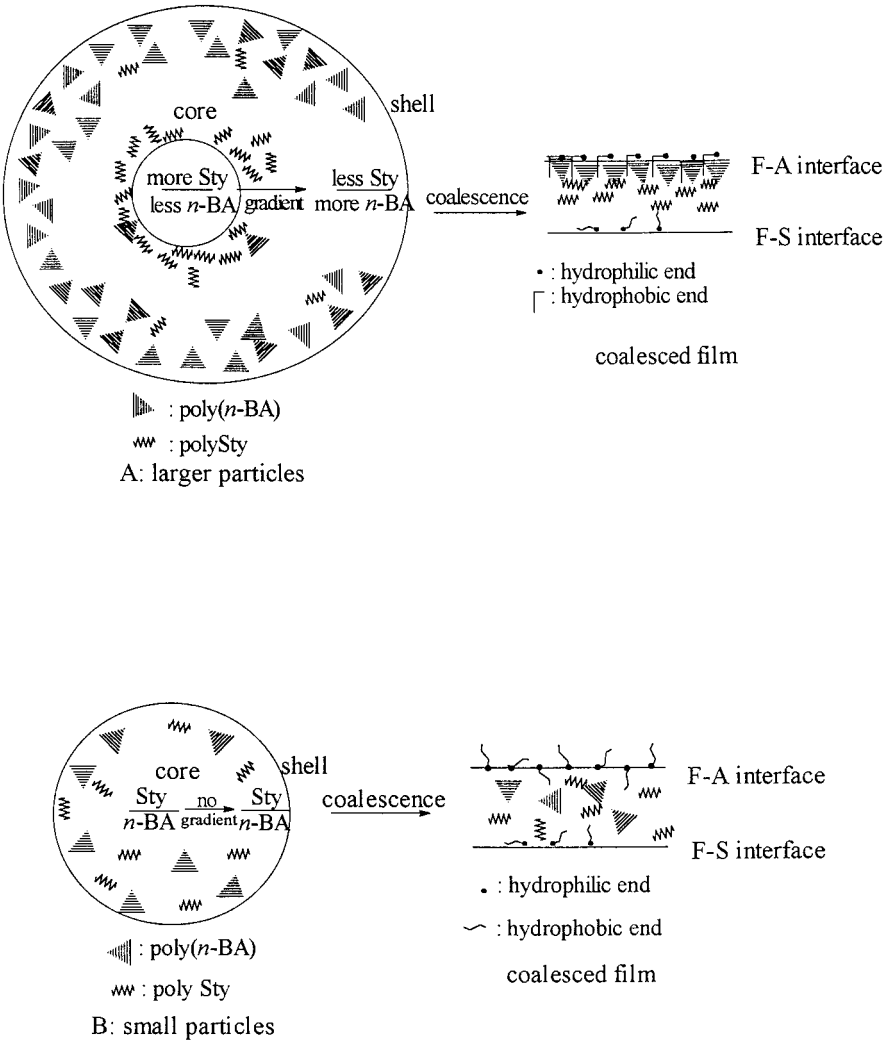

Figure 12 Schematic diagrams of core–shell effect in Sty/*n*-BA latex copolymers and latex film formation after coalescence: (A) larger particle size; (B) small particle size. (From Witucki, G. L., *J. Coat Tech.,* **65,** 57, © 1996 John Wiley & Sons, Inc., reproduced with permission.)

$$\beta = \varepsilon c \tag{5}$$

where ε (L mol^{-1} cm^{-1}) is the extinction coefficient, c (mol/L) is the concentration, and β (cm^{-1}) is the linear absorptivity. From the Beer–Lambert equation, the extinction coefficient is the slope of the linear absorptivity versus concentration. The extinction coefficients were calculated from Figure 18(A,B) for the 1056- and 1046-cm^{-1} band and are 0.14 and 1.9 L mol^{-1} cm^{-1} respectively. To quantify SDOSS at the interfaces, the absorbance index and reflective index spectra of SDOSS were incorporated into the penetration depth-profiling analysis. A schematic diagram of the algorithm developed for depth profiling is shown in Figure 19.[79]

According to eq. (1), the penetration depth depends upon the wavelength of electromagnetic radiation and the angle of incidence. Because eq. (1) was derived with an assumption that the examined specimens are homogeneous, any composition/concentration variations preclude the use of this useful relationship, especially if one is interested in the depth-profiling experiments. To apply this relationship, for quantitative analysis of nonhomogeneous surfaces, we developed an algorithm which allows us to overcome this problem.[60]

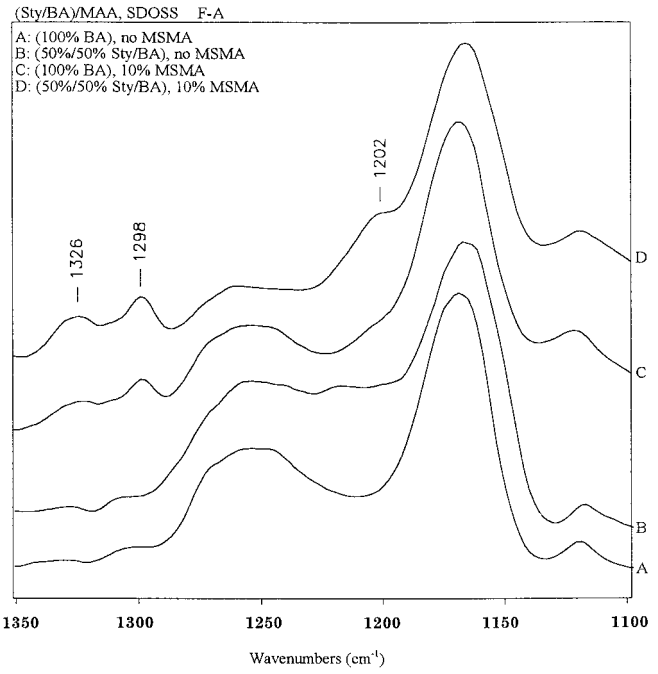

Figure 13 ATR FTIR spectra of various Sty/*n*-BA latex copolymers with and without MSMA in S—O asymmetric stretching vibrational modes at F–A interface: (A) 100% *n*-BA without MSMA; (B) 50/50% Sty/*n*-BA without MSMA; (C) 100% *n*-BA with MSMA; (D) 50/50% Sty/*n*-BA with MSMA. (From Witucki, G. L., *J. Coat Tech.,* **65,** 57, © 1996 John Wiley & Sons, Inc., reproduced with permission.)

In essence, a nonhomogeneous surface is numerically sliced to form a stack of parallel, thin homogeneous films. This is schematically illustrated in Figure 5. The surface is divided into n layers with each layer thickness, h_j. At the each boundary layer, L_j, the response of the sample to local evanescent waves can be characterized by a complex refractive index defined by $\hat{n}_j = n_j - ik_j$, where k_j is referred to as the absorption index.[60] By applying the Urban–Huang algorithm[60] to each layer, one can obtain information from each layer which is assumed to be homogeneous. This approach facilitates the use of eq. (1) to each layer, but the layers among themselves are not homogeneous. Using the approach of stacking all layers together, the surface is reconstructed by a stepwise treatment of the volumes occupied by each layer. This approach allows accurate quantitative analysis of surfaces, and its precision is determined by the number of spectra recorded at various depths.

Figures 20 and 21 illustrate a series of ATR FTIR spectra recorded as a function of the incidence angle, and it appears that the 1056-, 1050-, and 1046-cm^{-1} bands change intensities as a function of the angle of incidence. Using calibration curves shown in Figure 18(A,B) and the algorithm shown in Figure 19, Figure 22 was constructed. Curves F–A and F–S in Figure 22 are the concentration changes of SDOSS plotted as a function of the penetration depth near the F–A and F–S interfaces.

These data illustrate that the SDOSS concentration diminishes very rapidly at shallow depths. However, it levels off when the penetration depth approaches 1.9 μm. The highest concentrations, 1.25×10^{-4} and 1.01×10^{-4} mmol, near the F–A and F–S interfaces, respectively, are detected at the depth penetrations near 0.58 μm. These values diminish to about 0.25×10^{-4} and 0.2×10^{-4} mmol at around 1.9 μm from the F–A and F–S interfaces, respectively. To minimize the interfacial surface tension, SDOSS molecules exude toward the interfacial regions, and the highest concentrations are detected close to the F–A and F–S interfaces, but the SDOSS concentration decreases at greater depths.

Curves F–A and F–S of Figure 22 show that the SDOSS concentrations near the F–A interface are higher than those at the F–S interface. This behavior can be attributed to the ability of SDOSS molecules to migrate preferentially to-

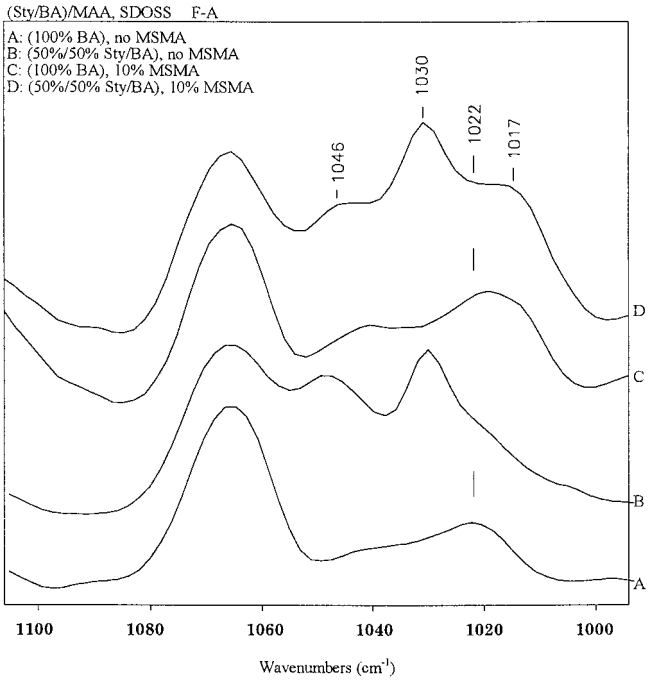

Figure 14 ATR FTIR spectra of various Sty/*n*-BA latex copolymers with and without MSMA in S—O symmetric stretching vibrational modes at F–A interface: (A) 100% *n*-BA without MSMA; (B) 50/50% Sty/*n*-BA without MSMA; (C) 100% *n*-BA with MSMA; (D) 50/50% Sty/*n*-BA with MSMA. (From Witucki, G. L., *J. Coat Tech.,* **65,** 57, © 1996 John Wiley & Sons, Inc., reproduced with permission.)

ward the F–A interface. Our previous studies[35,36] also indicated that SDOSS migrations are influenced by the surface tension of a substrate and the glass transition temperature (T_g) of the polymer/copolymer. For a higher styrene content, the T_g is higher, and the rate of latex coalescence increases. The latter results from the increase water evaporation, likely due to a hydrophobic nature of styrene. Because SDOSS is water-soluble, it will be carried out to the F–A interface. In this case, the effect of surface tension of a substrate on "trapping" surfactant near the F–S interface is small. As a result, the higher SDOSS concentration is detected near the F–A interface. However, when another latex layer modified with an MSMA is added, the distribution of SDOSS within this new layer is affected by an addition of the MSMA molecules.

STEP-SCAN PHOTOACOUSTIC DEPTH PROFILING

It is well documented that by changing the modulation frequency of an FTIR interferometer equipped with a photoacoustic cell it is possible to obtain information from various surface depths.[65] Step-scan PAS FTIR spectra recorded from the F–S interface of a 50%/50% Sty/*n*-BA latex film, using 400-, 300-, 200-, and 100-Hz phase modulation frequencies, are shown in Figure 23, traces A–D, respectively. Trace A, recorded at 400 Hz, shows two weak bands at 1056 and 1046 cm^{-1} which are due to the SO_3^- $Na^+\cdots HOOC$ and SO_3^- $Na^+\cdots H_2O$ associations, respectively.[80]

However, when the modulation frequency is decreased to 100 Hz, the 1056- and 1046-cm^{-1} bands decrease and eventually become nondetectable (trace D). At the same time, a new band at 1050 cm^{-1}, which is due to the symmetric S—O vibrations of free SO_3^- Na^+ hydrophilic end groups, is present at low modulation frequencies. This band dominates the spectra recorded with 100 Hz (Fig. 23, trace D). Since the depth of penetration of IR light is inversely proportional to the PM frequency,[81] for the 400-Hz PM frequency, the depth of penetration is shallowest. To estimate penetration depths at these modulation frequencies, eq. (3) can be utilized. Using the value of $\alpha = 1.57 \times 10^{-3}$ cm^2/s,[82] the penetration depths

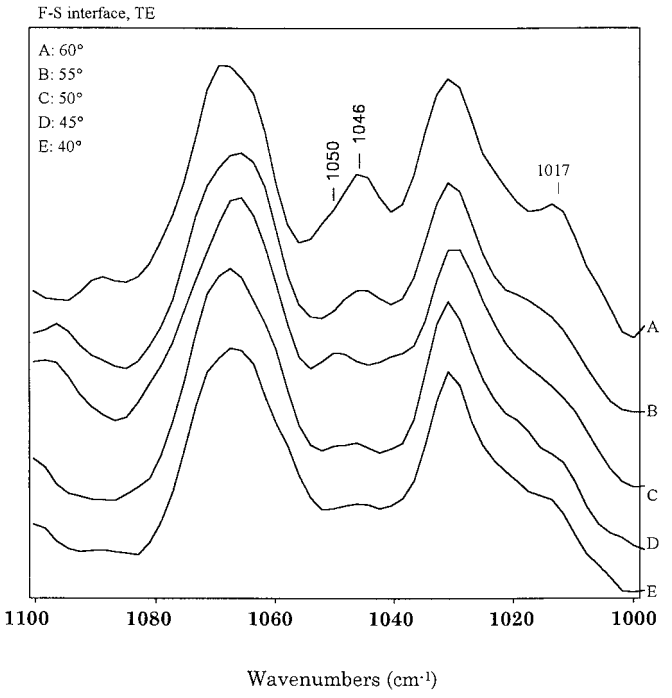

Figure 15 ATR FTIR spectra of S—O symmetric stretching vibrational modes of 50/50% Sty/*n*-BA composition containing 10% MSMA with various incident angle of IR light at F–S interface with TE polarization: (A) 60°; (B) 55°; (C) 50°; (D) 45°; (E) 40°. (From Niu, B.-J., and Urban, M. W., *J. Appl. Polym. Sci.,* **60,** 389, © 1996 John Wiley & Sons, Inc., reproduced with permission.)

at the examined frequencies were determined and are summarized in Table II. Based on the data shown in Figure 23, traces A–D, a higher content of nonbonded SO_3^- Na^+ hydrophilic end groups exist at the greater depths near the F–S interface. This is because water evaporates from the latex film, resulting in fewer water molecules trapped at greater depths. Therefore, there are fewer chances for SO_3^- Na^+ hydrophilic end groups to associate with H_2O and COOH groups. However, the presence of the 1056- and 1046-cm^{-1} bands is detected at the shallower depths, indicating that there are traces of water molecules near the F–S interface.

Figure 24(I–IV) illustrates a series of *I* and *Q* spectra recorded from the F–S interface, in 10° increments, at 400, 300, 200, and 100 Hz, respectively. In this experimental setup, the PM angle is 0°: Thus, the *Q* (0° phase) spectrum represents the signal from deeper penetration depths. As shown in Figure 24(I), the bands at 1056 and 1046 cm^{-1} gradually increase as the phase angle goes from 0° (*Q*) to 90° (*I*), indicating that within the first 11-μm layer from the F–S interface the distribution of SDOSS molecules is not homogeneous.

In a series of the step-scan spectra shown in Figure 24(II), a 300-Hz PM frequency was used. Although the bands at 1056, 1050, and 1046 cm^{-1} are detected, the band intensities at 1056 and 1046 cm^{-1} decrease to minimum, and the 1050-cm^{-1} band increases as the phase angles change from 90° (*I*) to 0° (*Q*). This observation indicates again that the SDOSS molecules are not uniformly distributed near a 13-μm layer from the F–S interface. Since water evaporation is one of the major driving forces during coalescence, at these depths from the F–S interface, the kinetics of the film formation may be different. The amount of water molecules decreases as penetration depths increase; therefore, the 1050-cm^{-1} band becomes detectable within a 13-μm layer, and the band at 1046 cm^{-1} due to the SO_3^- $Na^+ \cdots H_2O$ association decreases to become nondetectable at 0° (*Q*).

When the modulation frequency is set at 200 Hz, the bands at 1056 and 1046 cm^{-1} are not detected, and only the 1050-cm^{-1} band is present. This is shown in a series of spectra in Figure 24(III). The band at 1050 cm^{-1} is strongest for 0° (*Q*) phase angle and decreases as the phase angle goes to 90° (*I*). Similar trends for the band at

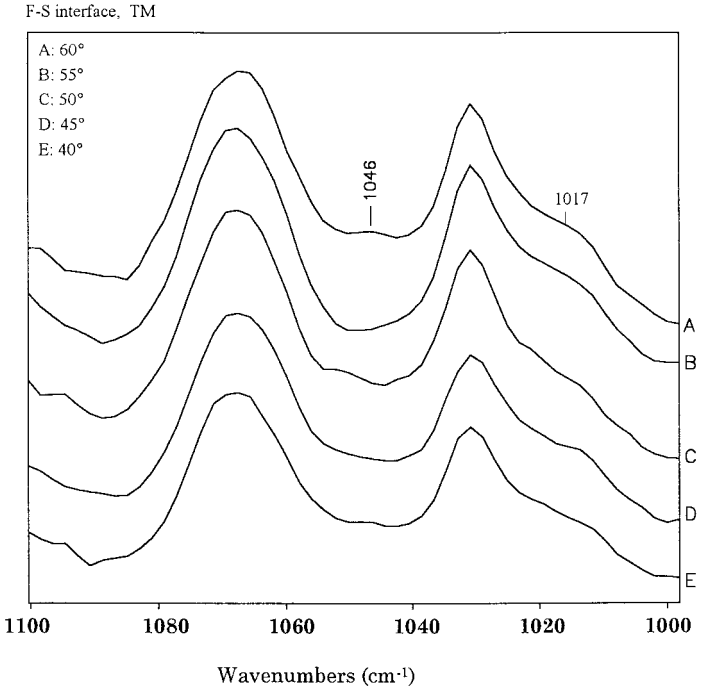

Figure 16 ATR FTIR spectra of S—O symmetric stretching vibrational modes of 50/50% Sty/*n*-BA composition containing 10% MSMA with various incident angle of IR light at F–S interface with TM polarization: (A) 60°; (B) 55°; (C) 50°; (D) 45°; (E) 40°. (From Niu, B.-J., and Urban, M. W., *J. Appl. Polym. Sci.,* **60,** 389, © 1996 John Wiley & Sons, Inc., reproduced with permission.)

1050 cm^{-1} are detected for 100-Hz modulation frequency with 0° and 90° phase angles at the F–S interface. These spectra are shown in Figure 24(IV). Again, these observations indicate that fewer of SDOSS molecules are present at the greater depths from the F–S interface. Having identified spectral features near the F–S interface, let us analyze the F–A interface: The step-scan photoacoustic FTIR spectra recorded with 400-, 300-, 200-, and 100-Hz modulation frequencies at the F–A interface are shown in Figure 25, traces A–D, respectively. Similarly to the discussion above, the depths of penetration for 400, 300, 200, and 100 Hz of PM frequencies are 11, 13, 16,

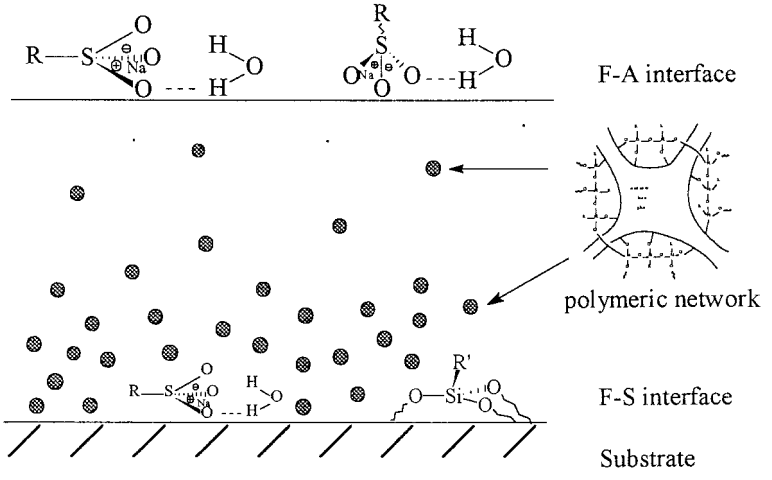

Figure 17 Schematic diagram of SDOSS and MSMA molecular arrangements.

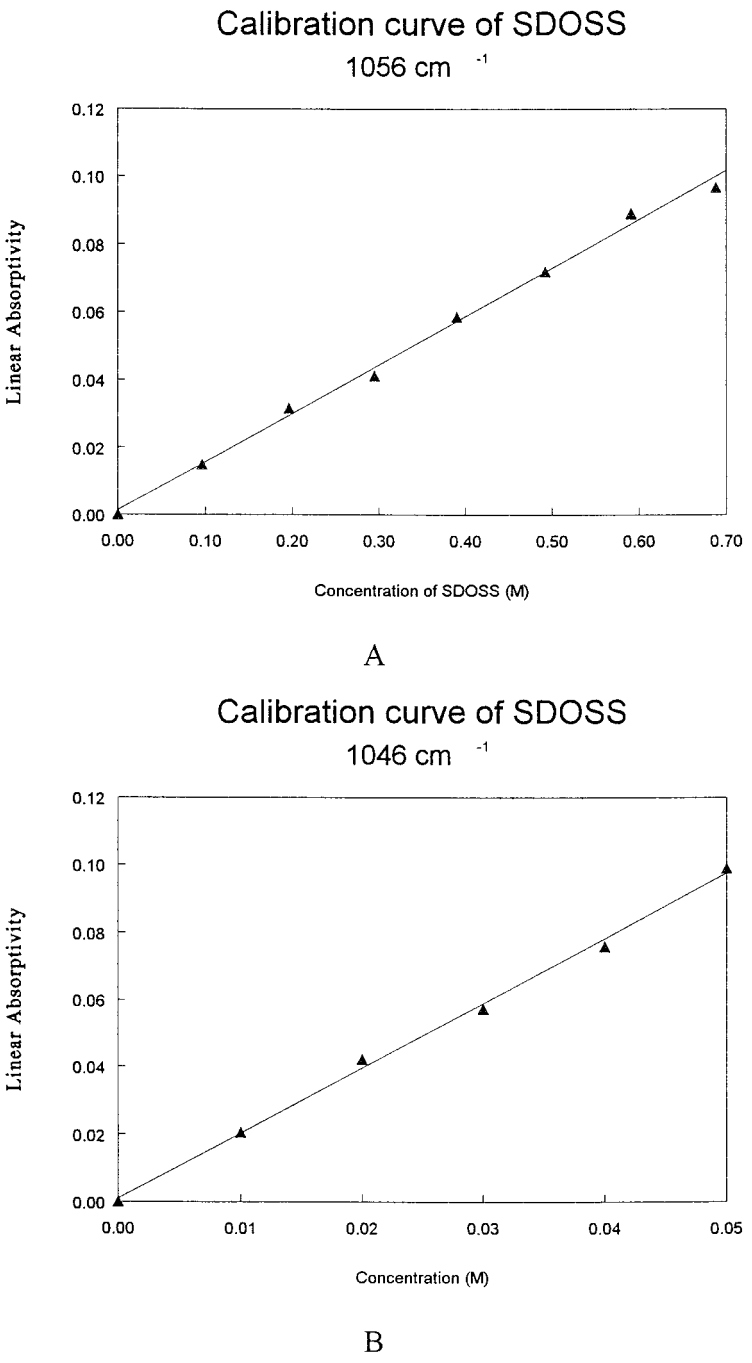

Figure 18 Calibration curves of linear absorptivity versus concentration of SDOSS: (A) 1056-cm^{-1} and (B) 1046-cm^{-1} bands. (From Niu, B.-J., and Urban, M. W., *J. Appl. Polym. Sci.,* **60,** 389, © 1996 John Wiley & Sons, Inc., reproduced with permission.)

and 22 μm, respectively. The 1056- and 1046-cm^{-1} bands are the strongest for 400 Hz (trace A). However, both decrease as the PM frequency decreases and become almost nondetectable above 200-Hz PM (traces C and D). Instead, the 1050 cm^{-1} band due to nonbonding SO_3^- Na^+ hydrophilic end groups on SDOSS is detectable at 200 Hz.

Since the 1056- and 1046-cm^{-1} bands are not detected at greater depths into the F–A interface, there are fewer H-bonding associations between SO_3^- Na^+ and water, and no interactions among SO_3^- Na^+ hydrophilic ends, water, and COOH groups are present. The 1056- and 1046-cm^{-1} bands, however, are detected at the shallower

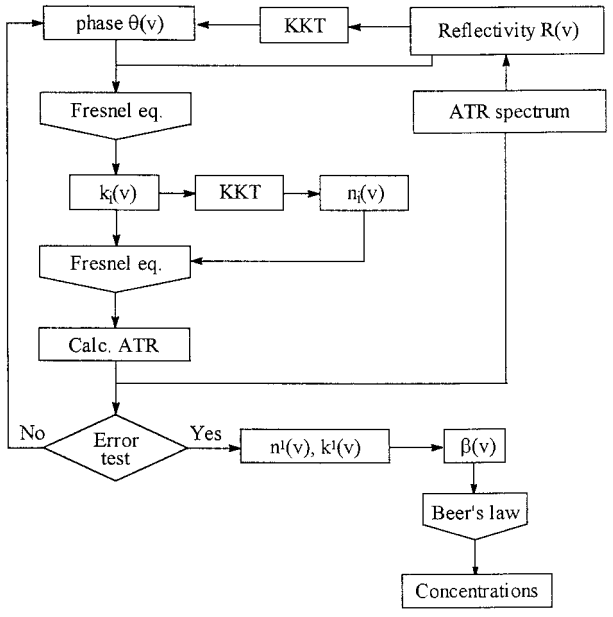

Figure 19 A schematic diagram of algorithm of penetration depth-profiling analysis.

depths; and the 1050-cm^{-1} band is detected deeper into the F–A interface. Due to equilibrium between inner water molecules, which evaporate from the film, and atmospheric water, which diffuse into the film, the film formation near the F–A interface is slower.

Figure 26(I–IV) illustrates a series of step-scan FTIR spectra recorded from the F–A interface at 400-, 300-, 200-, and 100-Hz modulation frequencies, with 90° (*I*) and 0° (*Q*) phase angles in 10° increments. As shown in Figure 26(I), while the band at 1046 cm^{-1} remains constant, the 1056-cm^{-1} band decreases as the phase angle changes from 0° (*Q*) to 90° (*I*). This observation indicates that water molecules are present near a 11-μm layer from the F–A interface and form SO_3^- $Na^+ \cdots H_2O$ associations. On the other hand, the strongest band intensity at 1056 cm^{-1} is detected in a 0° spectrum (*Q*), and as the phase angle increases, this band decreases, indicating that more acid groups are present near a 11-μm layer of the F–S interface. This behavior is attributed to the fact that water molecules are trapped near this interface, while the acid groups are closer to the deeper portions of the 11-μm layer.

Similarly, the same trends are found in the spectra recorded with 300 Hz [Fig. 26(II)]. However, the 1046 cm^{-1} band intensity decreases as

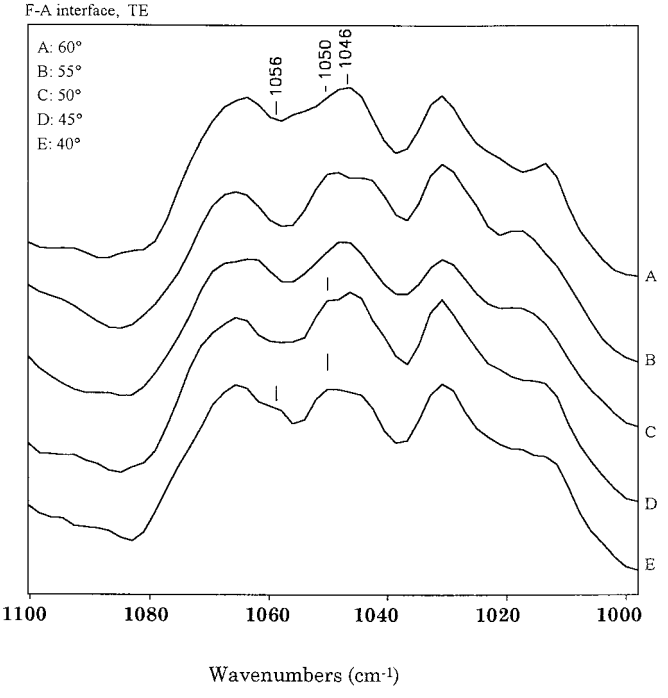

Figure 20 ATR spectra of the S—O symmetric stretching region with a series of angle of incidence at the F–A interface: (A) 60°; (B) 55°; (C) 50°; (D) 45°; (E) 40°. (From Niu, B.-J., and Urban, M. W., *J. Appl. Polym. Sci.,* **60,** 389, © 1996 John Wiley & Sons, Inc., reproduced with permission.)

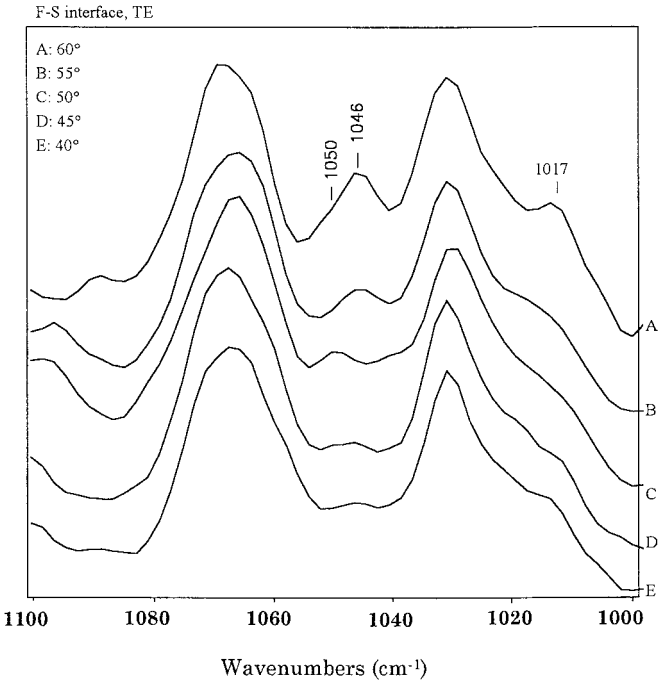

Figure 21 ATR spectra of the S—O symmetric stretching region with a series of angle of incidence at the F–S interface: (A) 60°; (B) 55°; (C) 50°; (D) 45°; (E) 40°. (From Niu, B.-J., and Urban, M. W., *J. Appl. Polym. Sci.,* **60,** 389, © 1996 John Wiley & Sons, Inc., reproduced with permission.)

the phase angle decreases. Hence, at greater depths, fewer water molecules are present, thus inhibiting SO_3^- $Na^+ \cdots H_2O$ associations. Again, a weak band intensity at 1056 cm^{-1} is detected for 0° spectrum (Q). Since water evaporates toward the film surface interface, more water molecules are able to stay in shallower penetration depths. Based on these spectra recorded from a 13-μm layer near the F–S interface, concentrations of water molecules increase parallel with the evaporation direction and decrease at greater penetration depths. Similar trends are observed near the F–A interface for modulation frequencies at 200 and 100 Hz, which are shown in Figure 26(III,IV), respectively. In this case, the 1050-cm^{-1} band is detected above a 16-μm layer and decreases at

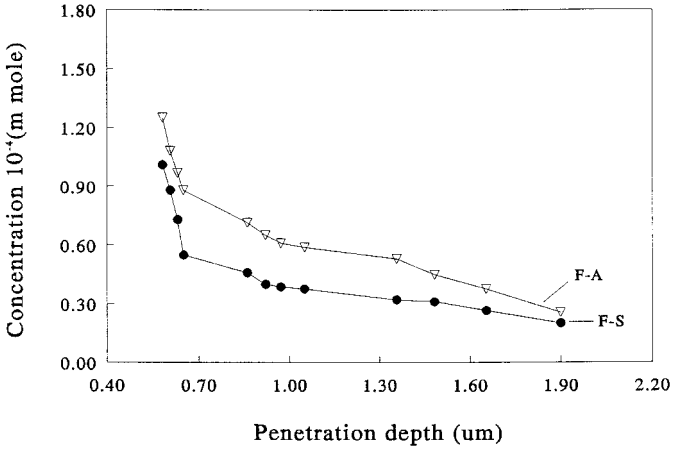

Figure 22 A plot of quantitative amount of SDOSS molecules versus depth penetration at the F–A and F–S interfaces.

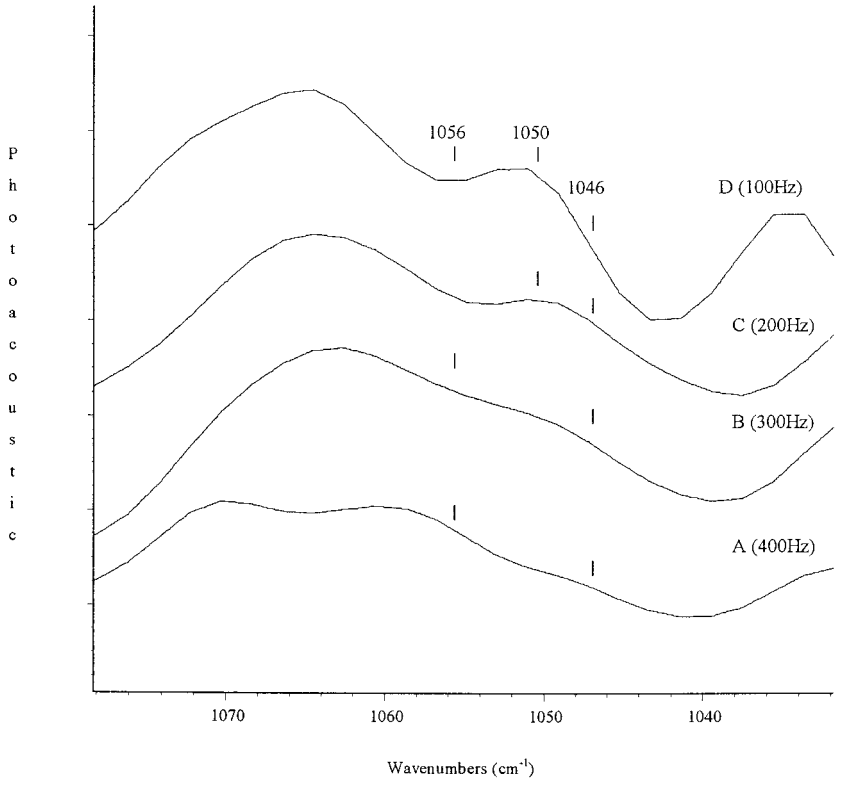

Figure 23 Step-scan PAS FT–IR spectra recorded at different modulation frequencies near the F–S interface: (A) 400 Hz; (C) 200 Hz; (D) 100 Hz. (Reproduced with permission from ref. 79. Copyright 1996 American Chemical Society.)

greater depths, indicating that there are no SDOSS molecules beyond a 22-μm boundary layer. In summary, spectroscopic data recorded from the F–S and F–A interfaces indicate that SDOSS molecules exude toward the F–A and F–S interfaces and are not homogeneously distributed across the film. Since 50% of Sty was incorporated into the latex particle composition, hydrophobicity is enhanced, resulting in faster rates of expelling water from latex particle interstices during coalescence. This is why free SDOSS at about 13 μm from the F–S interface is detected. Because water molecules are trapped near the F–S interfacial region, lower quantities are detected near 11 μm from the F–S interface. In addition, only the 1050-cm^{-1} band is detected beyond the 13-μm layer, indicating that coalescence is complete below 13 μm from the F–S interface. At the F–A interface, water molecules from the atmosphere are able to diffuse into the surface areas during coalescence; thus, SO_3^- $Na^+\cdots H_2O$ associations are detected at 11-, 13-, and 16-μm layers from the F–A interface. Similarly, coalescence is complete, and latex forms a continuous phase below 16 μm from the F–A interface.

Table II Penetration Depths at Various Modulation Frequencies

	Modulation Frequency (ω)			
	400 Hz	300 Hz	200 Hz	100 Hz
Penetration depths (μ_{th})	11μm	13μm	16μm	22μm

The plots of the band areas as a function of penetration depths are shown in Figures 27 and 28 for the F–S and F–A interfaces, respectively. In Figure 27, the content of the SO_3^- $Na^+\cdots H_2O$ associations (1046 cm^{-1}) decreases exponentially as penetration depths increase. This observation illustrates that water molecules trapped near the F–S interface become associated with the latex particles, thus affecting coalescence. However, the amount of the SDOSS molecules forming SO_3^- $Na^+\cdots COOH$ associations (1056 cm^{-1}) remain constant throughout a 9-μm layer, but the con-

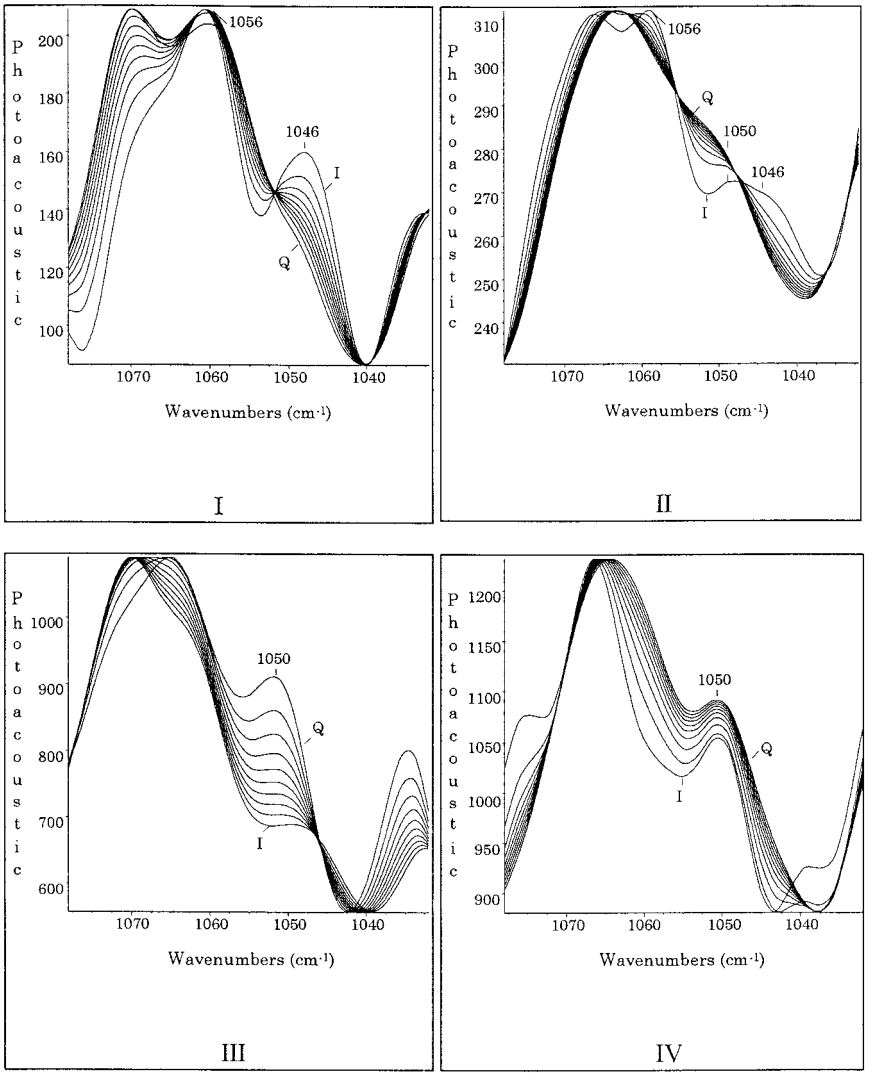

Figure 24 Ten steps of step-scan PAS FTIR spectra recorded at various modulation frequencies with *Q* (0°) and *I* (90°) phase angles near the F–S interface: (I) 400 Hz; (II) 300 Hz; (III) 200 Hz; (IV) 100 Hz. (Reproduced with permission from ref. 79. Copyright 1996 American Chemical Society.)

centration of the SO_3^- $Na^+\cdots$COOH associations significantly decreases as the penetration depths increase to become non-detectable above 11 μm from the F–S interface. Thus, at approximately 11 μm, the majority of the SO_3^- $Na^+\cdots$COOH associations are present. This behavior is attributed to the fact that the acid groups of the latex copolymer tend to migrate toward the interfacial region to alleviate interfacial surface tension near the F–S interface.[32] In addition, the relative amount of nonbonded SDOSS molecules (1050 cm^{-1}) becomes detectable at approximately 8.5 μm and gradually increases while going further away from the F–S interface. It appears that these nonbonding SDOSS molecules achieve a maximum concentration at approximately 14.5 μm, and their concentration decreases at greater penetration depths to become non-detectable at 22 μm. This observation indicates that there are no SDOSS molecules near the center portion of the film.

Figure 28 shows relative intensities of the bands responsible for SO_3^- $Na^+\cdots H_2O$, SO_3^- $Na^+\cdots$COOH, and nonbonding SDOSS associations near the F–A interface. It appears that according to the results presented in Figure 28 the relative amounts of SO_3^- $Na^+\cdots H_2O$ decrease exponentially with the increasing penetration

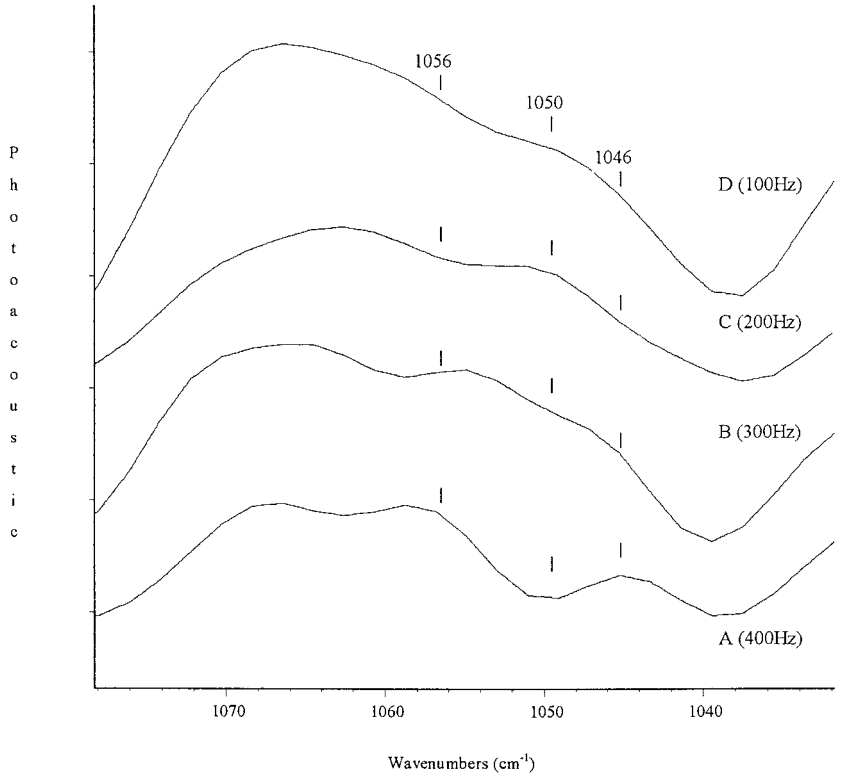

Figure 25 Step-scan PAS FTIR spectra recorded at different modulation frequencies near the F–A interface: (A) 400 Hz; (B) 300 Hz; (C) 200 Hz; (D) 100 Hz. (Reproduced with permission from ref. 79. Copyright 1996 American Chemical Society.)

depths (8.5 μm), followed by its decrease. At 13 μm, they become almost nondetectable, indicating that fewer water molecules penetrate into the surface of the latex film from the atmosphere, resulting in a higher concentration of SO_3^- $Na^+\cdots H_2O$ associations near a 8.5-μm layer. However, there are fewer water molecules beyond 8.5 μm, thus resulting in a significant decrease of the relative amounts of SO_3^- $Na^+\cdots H_2O$ associations near a 8.5-μm layer. However, there are fewer water molecules beyond 8.5 μm, thus resulting in a significant decrease of the relative amounts of SO_3^- $Na^+\cdots H_2O$ associations. Again, the amounts of SO_3^- $Na^+\cdots$COOH associations decrease as the penetration depths increase, and the presence of SO_3^- $Na^+\cdots$COOH becomes nondetectable at 13 μm from the F–A interface. At the same time, analysis of the F–S interface shows that the content of the SO_3^- $Na^+\cdots$COOH associations is higher; thus, the acid groups preferentially migrate toward the F–S interface to alleviate interfacial surface tension between Sty/*n*-BA latex film and a PTFE substrate.

Nonbonded SDOSS molecules are detected at approximately 12 μm from F–A interface, followed by their increase at greater penetration depths, and achieve maximum at approximately 16 μm. This increase is followed by a gradual decrease, which, at 22 μm, becomes nondetectable, and no nonbonding SDOSS molecules are found. Similarly, analysis of the F–S interface indicates that the nonbonding SDOSS molecules are detected at shallower depths than their counterparts at the F–A interface. This behavior is attributed to the water molecules which diffuse through the F–A interface from the atmosphere to form SO_3^- $Na^+\cdots H_2O$ associations. A comparison of the data shown in Figures 27 and 28 also indicates that the amount of SDOSS molecules near the F–A interface is approximately twice as large as that at the F–S interface.

Based on the data presented in this study, surfactant distribution may be divided into three zones: F–A interface, central region, and F–S interface. One of the surfactant properties is that it tends to migrate to the interfaces, minimizing the effect of the interfacial surface tension. In previous studies,[29] we illustrated that the surfactant migration is influenced by the surface tension of the substrate. In this case, latex films were cast

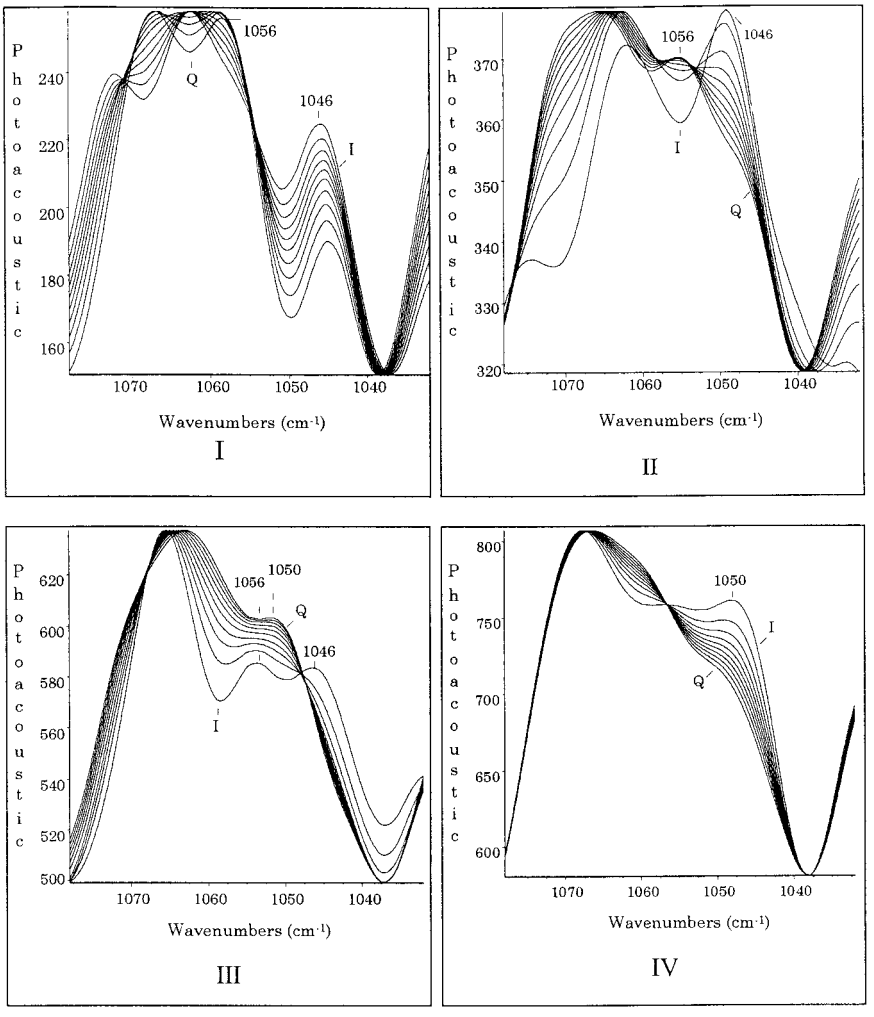

Figure 26 Ten steps of step-scan PAS FTIR spectra recorded at various modulation frequencies with *Q* (0°) and *I* (90°) phase angles near the F–A interface: (I) 400 Hz; (II) 300 Hz; (III) 200 Hz; (IV) 100 Hz. (Reproduced with permission from ref. 79. Copyright 1996 American Chemical Society.)

on polytetrafluoroethylene (PTFE), with the initial interfacial surface tension γ_{int} (H_2O–PTFE) equal to 50 mN/m and the surface tension of the latex polymer approximately 36.9 mN/m. As coalescence progresses, water evaporates, leaving the copolymer film in contact the PTFE substrate, forming a solid–solid interface.

Using the concept of interfacial surface tension expressed[83] by $\gamma_{int} = \gamma_{sub} + \gamma_{film} - 2(\gamma^d_{sub}\gamma^d_{film})^{1/2}$, the interfacial surface tension between the latex film and a PTFE substrate changes by 1.8 mN/m.[27,80] In this equation, γ_{int} is the interfacial surface tension, γ_{sub} and γ_{film} are the critical surface tensions of the substrate and the polymeric film, respectively, and γ^d_{sub} and γ^d_{film} are the dispersion components of the substrate and polymeric film, respectively. Due to a higher surface tension at the initial stages of coalescence, the surfactant molecules migrate to the F–S interface, but more surfactant molecules migrate toward the F–A interface due to water flux and to lower interfacial surface tension between the polymeric film and the substrate. Therefore, surfactant molecules cumulate near the F–A and F–S interfacial regions.

Since there are three different types of SDOSS interactions with the latex components: SO_3^- $Na^+\cdots H_2O$, SO_3^- $Na^+\cdots$HOOC, and free SDOSS molecules, one can follow latex film formation by monitoring SDOSS behavior during coalescence. Let us return to the step-scan IR spectra recorded with 400 Hz of modulation frequency near F–S

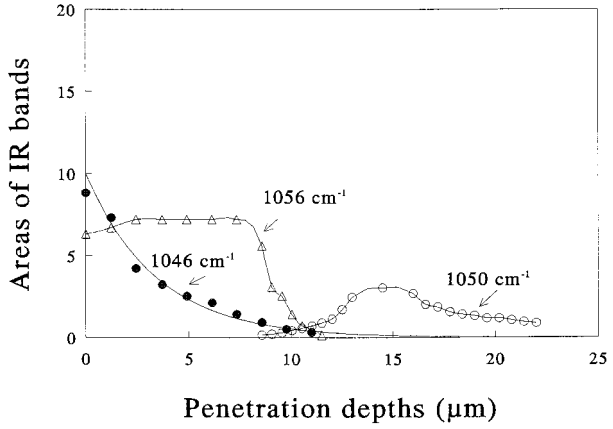

Figure 27 A plot of relative quantities of SDOSS with various associations as a function of penetration depths at the F–S interface. (Reproduced with permission from ref. 79. Copyright 1996 American Chemical Society.)

interface, which corresponds to the penetration depths near 11 μm. Because the band at 1046 cm^{-1} is detected, $SO_3^- Na^+ \cdots H_2O$ associations are present between the particle interstices. Furthermore, the presence of the 1056-cm^{-1} band indicates that the particle interdiffusion is not complete, because molecules have not completely evaporated from this layer.

This is schematically illustrated in Figure 29, which shows the F–S interface near the 11-μm layer. At approximately 13 μm from the F–S interface, there is a transition zone from the wet to dry stage of coalescence. In this transition layer,

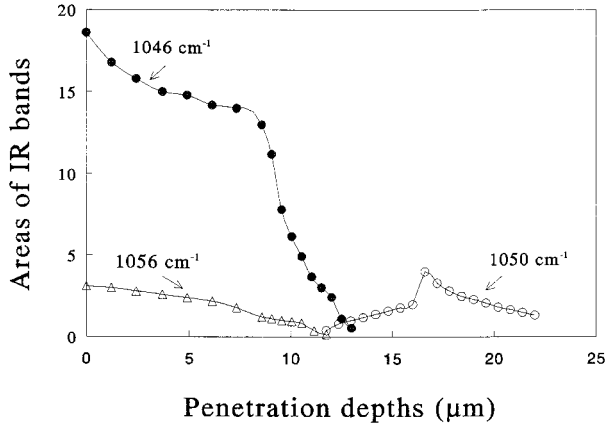

Figure 28 A plot of relative quantities of SDOSS with various associations as a function of penetration depths at the F–A interface. (Reproduced with permission from ref. 79. Copyright 1996 American Chemical Society.)

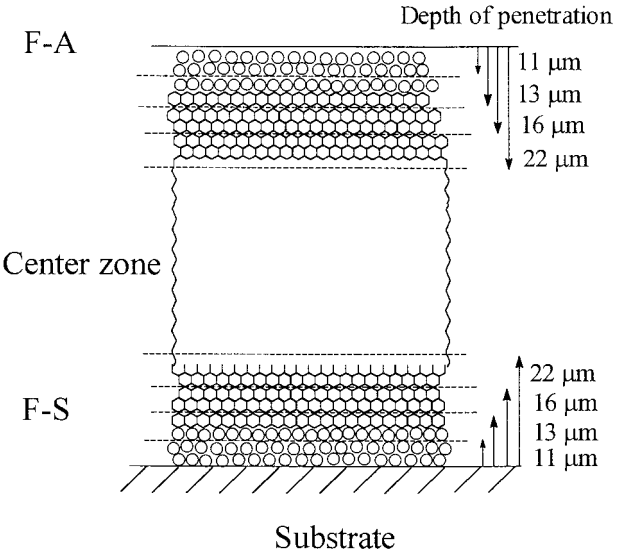

Figure 29 Schematic diagram of the film formation and depth penetration in coalesced latex film. (Reproduced with permission from ref. 79. Copyright 1996 American Chemical Society.)

polymer particles are not completely interdiffused, and at approximately 16 μm from the F–S interface, only the 1050-cm^{-1} band is detected [Fig. 24(III)], indicating no $SO_3^- Na^+ \cdots H_2O$ associations. As we recall the data presented in Figure 24(IV) and recorded from a 16-μm layer near the F–S interface, only the 1050-cm^{-1} band was detected, indicating that Sty/*n*-BA formed a continuous phase. However, in the case of the F–A interface, the presence of water in the surrounding atmosphere allows diffusion into the film, which could affect kinetics of the coalescence, resulting in significantly larger amounts of $SO_3^- Na^+ \cdots H_2O$ associations at shallower penetration depths, whereas the nonbonding SDOSS molecules are at deeper penetration depths.

The authors would like to thank National Science Foundation Coating Center for financial support of this work.

REFERENCES

1. J. W. Vanderhoff, *Br. Polym. J.,* **2,** 161 (1970).
2. R. E. Dillon, L. A. Matheson, and E. B. Bradford, *J. Colloid Sci.,* **6,** 108 (1951).
3. G. L. Brown, *J. Polym. Sci.,* **22,** 423 (1956).
4. T. F. Protzman and G. L. Brown, *J. Appl. Polym. Sci.,* **4,** 81 (1960).

5. E. M. Bocar, B. C. Dionne, Z. Fu, B. Kirk, P. M. Lesko, and A. D. Koller, *Macromolecules,* **26,** 5772 (1993).
6. O. Pekcan, *Trends Polym. Sci.,* **2,** 236 (1994).
7. Y. Wang and M. A. Winnik, *J. Phys. Chem.,* **97,** 2507 (1993).
8. J. L. Keddle, P. Meredith, R. A. L. Jones, and A. M. Donald, *Macromolecules,* **28,** 2673 (1995).
9. A. Haas-Bar Ilan, I. Noda, L. A. Schechtman, and Y. Talmon, *Macromolecules,* **33,** 2043 (1991).
10. Y. Wang, D. Hugue, M. A. Winnik, O. M. Leung, and M. C. Goh, *Langmuir,* **8,** 760 (1992).
11. D. Juhue and J. Lang, *Langmuir,* **9,** 972 (1993).
12. K. Hahn, G. Ley, H. Schuller, and R. Oberthur, *Colloid Polym. Sci.,* **266,** 631 (1988).
13. A. R. Sanderson, T. L. Crowley, J. D. Morrison, M. D. Barry, T. Morton-Jones, and A. R. Rennie, *Langmuir,* **8,** 2110 (1992).
14. M. Joanicot, K. Wong, J. Marquet, and B. Cabane, *Macromolecules,* **26,** 3168 (1993).
15. M. A. Linne, A. Klein, L. H. Sperling, and G. D. Wignall, *J. Macromol. Sci. Phys. B.,* **27,** 181 (1988).
16. M. A. Linne, A. Klein, G. A. Miller, L. H. Sperling, and G. D. Wignall, *J. Macromol. Sci. Phys. B,* **27,** 217 (1988).
17. K. D. Kim, L. H. Sperling, A. Klein, and G. D. Wignall, *Macromolecules,* **26,** 4624 (1993).
18. O. Pekcan, M. A. Winnik, and M. D. Croucher, *Macromolecules,* **23,** 2673 (1990).
19. Y. Wang and M. A. Winnik, *Macromolecules,* **26,** 3147 (1993).
20. Y. Wang, C.-L. Zhao, and M. A. Winnik, *J. Chem. Phys.,* **95,** 2143 (1991).
21. C.-L. Zhao, Y. Wang, Z. Hruska, and M. A. Winnik, *Macromolecules,* **23,** 4082 (1990).
22. M. S. El-Asser and A. A. Robertson, *J. Paint Technol.,* **47,** 50 (1975).
23. Y. Chevalier, C. Pichot, C. Graillat, M. Joanicot, K. Wong, P. Lindner, and B. Cabane, *Colloid Polym. Sci.,* **270,** 806 (1992).
24. M. Joanicot, K. Wong, J. Maquet, Y. Chevalier, C. Pichot, C. Graillat, P. Lindner, L. Rios, and B. Cabane, *Prog. Colloid Polym. Sci.,* **81,** 175 (1990).
25. S. S. Voyutskii, *J. Polym. Sci.,* **32,** 528 (1958).
26. M. W. Urban and K. W. Evanson, *Polym. Commun.,* **31,** 279 (1990).
27. K. W. Evanson and M. W. Urban, *J. Appl. Polym. Sci.,* **42,** 2287 (1991).
28. K. W. Evanson, T. A. Thorstenson, and M. W. Urban, *J. Appl. Polym. Sci.,* **42,** 2297 (1991).
29. K. W. Evanson and M. W. Urban, *J. Appl. Polym. Sci.,* **42,** 2309 (1991).
30. T. A. Thorstenson and M. W. Urban, *J. Appl. Polym. Sci.,* **47,** 1381 (1993).
31. T. A. Thorstenson and M. W. Urban, *J. Appl. Polym. Sci.,* **47,** 1387 (1993).
32. T. A. Thorstenson, L. K. Tebelius, and M. W. Urban, *J. Appl. Polym. Sci.,* **49,** 103 (1993).
33. T. A. Thorstenson, L. K. Tebelius, and M. W. Urban, *J. Appl. Polym. Sci.,* **50,** 1207 (1993).
34. J. P. Kunkel and M. W. Urban, *J. Appl. Polym. Sci.,* **50,** 1217 (1993).
35. B.-J. Niu and M. W. Urban, *J. Appl. Polym. Sci.,* **56,** 377 (1995).
36. B.-J. Niu and M. W. Urban, *J. Appl. Polym. Sci.,* **60,** 371 (1996).
37. L. K. Tebelius and M. W. Urban, *J. Appl. Polym. Sci.,* **56,** 387 (1995).
38. S. S. Voyutskii and B. H. Starkh, *Colloid J. USSR,* **14,** 314 (1952).
39. H. Wagner and G. Fisher, *Kolloid Z.,* **77,** 12 (1936).
40. D. Juhue, Y. Wang, J. Lang, O. Leung, M. C. Goh, and M. L. Winnik, *J. Polym. Sci. Polym. Phys.,* **33,** 1123 (1995).
41. E. B. Bradford and J. W. Vanderhoff, *J. Macromol. Chem.,* **1,** 335 (1966).
42. E. B. Bradford and J. W. Vanderhoff, *J. Macromol. Sci. Phys. B,* **6,** 671 (1972).
43. J. W. Vanderhoff, E. B. Bradford, and W. K. Carrington, *J. Polym. Sci. Symp.,* **41,** 155 (1973).
44. B. J. Roulstone, M. C. Wilkinson, and J. Hearn, *Polym. Int.,* **27,** 43 (1992).
45. M. Okubo, T. Takeya, Y. Tsutumz, Y. Kapookat, and T. Matsumoto, *J. Polym. Sci. Polym. Chem. Ed.,* **19,** 1 (1981).
46. P. K. Isaacs, *J. Macromol. Chem.,* **1,** 163 (1966).
47. M. W. Urban, *Vibrational Spectroscopy of Molecules and Macromolecules on Surfaces,* Wiley-Interscience, New York, 1993, Chap. 1.
48. N. J. Harrick, *Internal Reflection Spectroscopy,* Interscience, New York, 1967.
49. J. L. Koenig, *Spectroscopy of Polymers,* American Chemistry Society, Washington, DC, 1992.
50. M. W. Urban, *Vibrational Spectroscopy of Molecules and Macromolecules on Surfaces,* Wiley-Interscience, New York, 1993, Chap. 3.
51. F. M. Mirabella, Jr., *Appl. Spectrosc. Rev.,* **21**(1,2), 45 (1985).
52. J. Fahrenfort, in *Proceedings of IVth International Meeting,* Bologna, 1959, Vol. 2, A. Mangini, Ed., Pergamon Press, London, 1962, p. 701.
53. J. Fahrenfort, *Spectrochim. Acta,* **17,** 698 (1961).
54. P. A. Wilks, Jr. and T. Hirschfeld, *Appl. Spectrosc. Rev.,* **1,** 99 (1967).
55. T. Hirschfeld, *Appl. Spectrosc.,* **21,** 335 (1967).
56. M. W. Urban and M. T. Stewart, *J. Appl. Polym. Sci.,* **39,** 265 (1990).
57. J. R. Hollahan and G. L. Carlson, *J. Appl. Polym. Sci.,* **14,** 2499 (1970).
58. M. Morra, E. Occhielo, R. Marloa, F. Garbassi, P. Humphrey, and D. Johnson, *J. Colloid Inter. Sci.,* **137,** 11 (1990).
59. J. B. Huang and M. W. Urban, *Appl. Spectrosc.,* **46,** 1666 (1992).
60. J. B. Huang and M. W. Urban, *Appl. Spectrosc.,* **47,** 973 (1993).

61. A. Rosencwaig, *Photoacoustics and Photoacoustic Spectroscopy,* Wiley-Interscience, New York, 1980, Chap. 9.
62. A. Rosencwaig and A. Gersho, *Science,* **190,** 556 (1975).
63. M. W. Urban, *J. Coat. Tech.,* **59**(745), 29 (1987).
64. M. W. Urban and J. L. Koenig, *Appl. Spectrosc.,* **40,** 994 (1986).
65. R. M. Dittmar, R. A. Palmer, and R. O. Carter III, *Appl. Spectrosc. Rev.,* **29,** 171 (1994).
66. R. A. Palmer, *Spectroscopy,* **8**(2), 26 (1993).
67. L. Bertrand, *Appl. Spectrosc.,* **42,** 134 (1988).
68. C. J. Manning, R. M. Dittmar, R. A. Palmer, and L. J. Chao, *Infrar. Phys.,* **33,** 53 (1992).
69. R. M. Ditmar, J. L. Chao, and R. A. Palmer, *Appl. Spectrosc.,* **45,** 1104 (1991).
70. R. A. Palmer and R. M. Dittmar, *Thin Solid Films,* **223,** 31 (1993).
71. V. G. Gregoriou, M. Daun, M. W. Schauer, J. L. Chao, and R. A. Palmer, *Appl. Spectrosc.,* **47,** 1311 (1993).
72. I. Noda, A. E. Dowrey, and C. Marcott, *Appl. Spectrosc.,* **47,** 1317 (1993).
73. T. Nakano, T. Yokoyama, and H. Toriumi, *Appl. Spectrosc.,* **47,** 1354 (1993).
74. E. P. Plueddemann, *Prog. Org. Coat.,* **11,** 297 (1983).
75. S. C. Kimand and L. H. Sperling, Eds., IPNs Around the World, *Science and Engineering,* Wiley, New York, 1997.
76. G. L. Witucki, *J. Coat. Tech.,* **65**(822), 57 (1993).
77. B.-J. Niu and M. W. Urban, *J. Appl. Polym. Sci.,* **60,** 389 (1996).
78. B.-J. Niu and M. W. Urban, *J. Appl. Polym. Sci.,* **62,** 1903 (1996).
79. M. W. Urban, *Vibrational Spectroscopy of Molecules and Macromolecules on Surfaces,* Wiley-Interscience, New York, 1993, Chap. 8.
80. B.-J. Niu, L. R. Martin, L. K. Tebelius, and M. W. Urban, in *Film Formation in Waterborne Coatings,* T. Provder, M. A. Winnik, and M. W. Urban, Eds., ACS Symposium Series 648, American Chemical Society, Washington, DC, 1996, Chap. 20.
81. A. Rosencwaig and A. Gersho, *J. Appl. Phys.,* **47,** 64 (1976).
82. A. Trainor, *Polymer,* **23,** 1108 (1982).
83. F. M. Fowkes, in *Treaties on Adhesion and Adhesives, Vol. I: Theory,* R. L. Patrick, Ed., Marcel Dekker, New York, 1967, Chap. 9.